

## FAR INFRARED *SPITZER* OBSERVATIONS OF ELLIPTICAL GALAXIES: EVIDENCE FOR EXTENDED DIFFUSE DUST

PASQUALE TEMI<sup>1,2</sup>, FABRIZIO BRIGHENTI<sup>3,4</sup>, WILLIAM G. MATHEWS<sup>3</sup>

*Draft version October 3, 2018*

### ABSTRACT

Far-infrared *Spitzer* observations of elliptical galaxies are inconsistent with simple steady state models of dust creation in red giant stars and destruction by grain sputtering in the hot interstellar gas at  $T \sim 10^7$  K. The flux at  $24\mu\text{m}$  correlates with optical fluxes, suggesting that this relatively hot dust is largely circumstellar. But fluxes at  $70\mu\text{m}$  and  $160\mu\text{m}$  do not correlate with optical fluxes. Elliptical galaxies with similar  $L_B$  have luminosities at  $70\mu\text{m}$  and  $160\mu\text{m}$  ( $L_{70}$  and  $L_{160}$ ) that vary over a factor  $\sim 100$ , implying an additional source of dust unrelated to that produced by ongoing local stellar mass loss. Neither  $L_{70}/L_B$  nor  $L_{160}/L_B$  correlate with the stellar age or metallicity. Optical line fluxes from warm gas at  $T \sim 10^4$  K correlate weakly with  $L_{70}$  and  $L_{160}$ , suggesting that the dust may be responsible for cooling this gas. Many normal elliptical galaxies have emission at  $70\mu\text{m}$  that is extended to 5–10 kpc. Extended far-infrared emission with sputtering lifetimes of  $\sim 10^8$  yrs is difficult to maintain by mergers with gas-rich galaxies. Instead, we propose that this cold dust is buoyantly transported from reservoirs of dust in the galactic cores which is supplied by mass loss from stars in the core. Intermittent energy outbursts from AGNs can drive the buoyant outflow.

*Subject headings:* galaxies: elliptical and lenticular; galaxies: ISM; infrared: galaxies; infrared: ISM

### 1. INTRODUCTION

The study of far-infrared (FIR) emission from elliptical galaxies is particularly interesting because the internal rates that dust is formed and destroyed can both be estimated. Dust is produced by mass loss from evolving red giant stars in the old stellar population typical of these galaxies. This mass loss is directly observed in the cumulative mid-infrared 10– $24\mu\text{m}$  emission from circumstellar regions around giant stars, causing the surface brightness profiles at 10– $24\mu\text{m}$  to resemble those at optical wavelengths (Knapp et al. 1989; Athey et al. 2002). The dust destruction rate by sputtering can be estimated from the frequency of thermal impacts from ions in the hot interstellar gas which for many ellipticals can be estimated from X-ray observations. During their sputtering lifetimes, dust grains ejected from giant stars are heated by starlight and thermal electron impacts to temperatures that radiate in the FIR (e.g. Tsai & Mathews 1995, 1996; Temi et al. 2003). This radiation has been observed both by the *Infrared Astronomical Satellite*, *IRAS* (Knapp et al. 1989) and by the *Infrared Space Observatory*, *ISO* (Temi et al. 2004). In addition, small optically obscuring clouds and disks of dusty gas have been detected in about half of the bright ellipticals studied with the *Hubble Space Telescope*, *HST* (van Dokkum & Franx 1995; Ferrari et al. 1999; Lauer et al. 2005). These clouds probably formed from dusty gas ejected from stars within the central  $\sim\text{kpc}$  in these

elliptical galaxies (Mathews & Brighenti 2003).

Galaxy mergers are another obvious possible source of dust in elliptical galaxies, indeed it is widely thought that ellipticals are formed by mergers. Elliptical-looking galaxies can be produced after a few Gyrs following the merger of two disk galaxies (e.g. Barnes & Hernquist 1992), but this simple recipe may not easily explain all structural and kinematic properties of these galaxies (Naab, Jesseit & Burkert 2006). Many of the mergers that produced the ripples, shells and counter-rotating cores in elliptical galaxies probably occurred a very long time ago. It is likely that massive boxy ellipticals, similar to many of those with strong FIR emission, have experienced mostly “dry” gas and dust-free mergers during the last few Gyrs (Bell et al. 2004; Faber et al. 2006). Nevertheless, mergers do occasionally occur between low-redshift ellipticals and gas-rich galaxies and these post-merger ellipticals often selectively appear in the observing lists of infrared observers. Our previous study of FIR emission from elliptical galaxies was based on a sample chosen from the *ISO* data archive (Temi et al. 2004) that included a significant number of galaxies with abnormally large masses of dust and cold gas which are uncharacteristic of elliptical galaxies in general. The large range of FIR luminosities that we found in the *ISO* sample was therefore not unexpected, and it was reasonable to suppose that mergers with dusty galaxies explained the absence of correlations between optical and FIR emission. The failure to find correlations between the FIR and optical luminosities of elliptical galaxies has been used in the past to argue that the cold dust is acquired in a stochastic fashion by mergers (Forbes 1991).

To understand the relative role of internal and external sources of dust in elliptical galaxies, we describe here new *Spitzer* observations at 24, 70 and  $160\mu\text{m}$ . Our full sample consists of 46 elliptical galaxies, formed by combining our own proprietary *Spitzer* observations with those

<sup>1</sup> Astrophysics Branch, NASA/Ames Research Center, MS 245-6, Moffett Field, CA 94035.

<sup>2</sup> SETI Institute, Mountain View, CA 94043; and Department of Physics and Astronomy, University of Western Ontario, London, ON N6A 3K7, Canada.

<sup>3</sup> University of California Observatories/Lick Observatory, Board of Studies in Astronomy and Astrophysics, University of California, Santa Cruz, CA 95064.

<sup>4</sup> Dipartimento di Astronomia, Università di Bologna, via Ranzani 1, Bologna 40127, Italy.

of other observers. The improved sensitivity and angular resolution of *Spitzer* provides clear evidence that the  $70\mu\text{m}$  emission is spatially extended in many ellipticals. In particular, we find extended FIR emission in elliptical galaxies that do not contain uncharacteristically large masses of neutral, molecular or optically visible cold gas. The diffuse nature of the dust in these otherwise normal galaxies, combined with the relatively short (ion sputtering) lifetime for dust destruction in the hot gas, favors an internal source of dust rather than dust-rich mergers which are probably too infrequent. The luminosity of extended FIR dust emission in most ellipticals greatly exceeds that expected from normal mass loss from local stars. However, small, optically thick nuclear dust clouds observed in many elliptical galaxies may provide an alternative, more plausible source for the extended FIR dust emission. Consequently, we argue that dust accumulated in the central regions of elliptical galaxies from stellar sources in the core is transported out to larger radii by buoyantly rising gas intermittently heated by low-luminosity active galactic nuclei (AGN) in the galactic cores. If this hypothesis can be confirmed in more detail, the presence of extended cold dust can be used to trace the radial circulation of hot gas in these galaxy/groups. Such circulation flows are known to be consistent with X-ray observations in which very little hot gas cools to low temperatures (Mathews, Brighenti & Buote 2004).

## 2. THE SAMPLE

For this study we construct a sample of 46 elliptical galaxies by combining far-infrared *Spitzer* observations from our own *Spitzer* data with additional galaxies in the public *Spitzer* archive. Our proprietary far-infrared *Spitzer* observations of elliptical galaxies (PID 20171, PI P.Temi) consists of 11 non-peculiar, bright ( $L_B \geq 2 \times 10^{10} L_{B,\odot}$ ) elliptical galaxies, most having high-quality X-ray observations. Galactic proximity and spatial scale were also important factors in choosing this sample since high angular resolution is needed to separate emission from dusty cores and diffuse emission from truly interstellar dust spread over the galactic volume. Furthermore, we avoided sources with strong radio sources and AGN that have detectable signals in the far infrared. Ellipticals with strong infrared Milky Way cirrus or bright spiral galaxies in the vicinity were also avoided. Since one of our goals is to study the interaction between dust and hot gas, we included many galaxies for which the X-ray emission is well-studied by either *Chandra* or *XMM*.

In addition to our original sample we selected 35 additional ellipticals from data currently available in the public *Spitzer* archive targeted by several PIs during their General Observation in Cycles 1 and 2, Guaranteed Time Observations, and the Legacy Program SINGS (Kennicutt et al. 2003). All the galaxies added to our original sample were chosen using selection criteria tailored to our specific scientific goals. Thus, the 46 galaxies studied here form a rather homogeneous sample and is large enough to be statistically meaningful.

Tables 1 and 2 summarize the relevant properties of the sample galaxies including the far-infrared photometric measurements. Optical data are taken from the LEDA catalog (Paturel et al. 1997) and the RSA catalog (Sandage & Tamman 1981), while X-ray data are from Ellis and O’Sullivan et al. (2006). Luminosities and dis-

tances are calculated with  $H_0 = 70 \text{ km s}^{-1} \text{ Mpc}^{-1}$  and are derived from the flux densities in Table 1 using far-infrared (FIR) passbands of  $\Delta\lambda = 5.3, 19$  and  $34\mu\text{m}$  for emission at 24, 70 and  $160\mu\text{m}$  respectively. The PIs of the original *Spitzer* program from which the galaxies have been selected are shown in column two of Table 1. All galaxies are classified as ellipticals in the NED catalog, and the morphological type T is taken from the LEDA catalog. Nevertheless, we shall find that our sample contains some S0 galaxies. Most of the sample galaxies have known X-ray luminosities  $L_x$ , which are a measure of the hot gas present in each galaxy.

Of the 46 galaxies in the sample three are dwarf elliptical galaxies (NGC855, NGC1377, and NGC3265) with  $L_B \leq 5 \times 10^9 L_{B,\odot}$ . Although they are listed in Table 1, they are not included in our discussion.

## 3. OBSERVATIONS AND DATA REDUCTION

The data presented here were acquired with the Multi-band Imager Photometer (MIPS) (Rieke et al. 2004) on the *Spitzer Space Telescope* (Werner et al. 2004) in three wavebands centered at 24, 70 and  $160\mu\text{m}$ . Since the galaxy sample has been constructed by collecting archival data from several *Spitzer* observing programs, the image data were recorded using observing modes and integration times tailored for their original scientific goals. As a consequence, although the maps represent the deepest FIR images acquired to date, some data achieve sensitivities that are not always optimized for targets that are intrinsically faint at far-infrared wavelengths. For example, three of the brightest ellipticals in the Virgo Cluster (NGC4472, NGC4636, and NGC4649) recorded under a guaranteed time program (PID 69, PI G. Fazio) reach a relatively low sensitivity of 0.5MJy/sr and 1.1MJy/sr ( $1\sigma$ ) at 70 and  $160\mu\text{m}$ , respectively, while other galaxies (i.e. PID 20171, PI P. Temi) have deeper maps at a sensitivity level of only 0.12MJy/sr and 0.3MJy/sr for the same two wavebands. The SINGS data are recorded in MIPS scan mode, covering a very large sky area ( $\sim 30' \times 10'$ ), incorporating two separated passes at each source location. SINGS images correspond to maps with intermediate sensitivity. Details on the observing strategies, field coverage and integration times for the SINGS program are described by Kennicutt et al. (2003). Apart from the SINGS observations, data have been acquired in MIPS photometry mode, allowing appropriate coverage of the sources and their extended emission. At all wavelengths, sufficiently large field sizes were chosen to reliably measure the background emission. We used the Basic Calibrated Data (BCD) products from the *Spitzer* Science pipeline (version 13.2) to construct mosaic images for all objects. Pipeline reduction and post-BCD processing using the MOPEX software package (Makovoz et al. 2006) provide all necessary steps to process individual frames: dark subtraction, flat-fielding, mux-bleed correction, flux calibration, correction of focal plane geometrical distortion, and cosmic ray rejection.

Foreground stars and background galaxies were present in the final mosaiced images at all bands. These were identified by eye and cross-checked using surveys at other wavelengths (Digital Sky Survey and 2MASS). They were then masked out from each MIPS image before flux extraction was performed. Also, a few asteroids were identified and removed from the affected maps. Aperture

photometry was performed by measuring fluxes in suitable circular apertures around the centers. Flux densities were extracted from apertures extending out to the entire optical disk of each galaxy ( $R_{25}$ ). Sky subtraction was performed by averaging values from multiple apertures placed around the target, avoiding any overlap with the faint extended emission from the galaxy. Uncertainties in flux densities due to sky subtraction are generally less than 1%, but can be of the order of tens of percent for faint sources.

The measured flux densities are listed in Table 1. Most of the galaxies in the sample have been detected by MIPS, and among them a large fraction show far-infrared emission well beyond the sensitivity capabilities of previous infrared space observatories. Although most of the galaxies presented in this paper are unpublished either because they are our own proprietary data or because the analysis is still in progress by the original PIs, results for a few galaxies are already present in the literature (i.e. the SINGS galaxies). We find that our flux densities are in good agreement with previously published data. The only exception is the measured flux density at  $160\mu\text{m}$  reported by Dale et al. (2005) for the SINGS galaxy NGC584. Very likely this discrepancy is due to a misidentification of the target in their very large  $160\mu\text{m}$  scan map. Corrections for extended emission were applied to the fluxes as described in the Spitzer Observer’s manual. Photometric errors listed in Table 1 refer only to the statistical uncertainties. Total errors should include systematic uncertainties due to flux calibration and to sky subtraction errors. The uncertainties on the final absolute calibration are estimated at 10% for the  $24\mu\text{m}$  data, and 20% at 70 and  $160\mu\text{m}$ .

Figure 1 shows gray-scale images of a representative sub-sample of galaxies. The column of panels on the left is the  $24\mu\text{m}$  data, while 70 and  $160\mu\text{m}$  data are shown in the center and right columns, respectively. Galaxies are ordered by ascending IR flux in a common field of view of  $3' \times 3'$ . Some very faint galaxies are shown, including a non detection at  $160\mu\text{m}$  and few sources with extended far-infrared emission. Detailed images of the diffuse extended emission in NGC4636 and NGC5044 will be presented in a companion paper currently in preparation.

#### 4. COMPARISON OF FIR, OPTICAL AND X-RAY EMISSION

In Figure 2 we compare fluxes at 24, 70 and  $160\mu\text{m}$  with optical B-band fluxes and a related plot of FIR and B-band luminosities is shown in Figure 3. Both the  $24\mu\text{m}$  and B-band fluxes and luminosities are clearly correlated,

$$\log F_{24} = (8.37 \pm 0.42) + (0.716 \pm 0.043) \log F_{B,\odot} \quad (1)$$

and

$$\log L_{24} = (32.37 \pm 0.69) + (0.799 \pm 0.066) \log L_{B,\odot}. \quad (2)$$

The approximate consistency with unit slope  $F_{24} \propto F_B$  indicates that the emission at  $24\mu\text{m}$ , like that at mid-IR wavelengths (Knapp et al. 1989; Athey et al. 2002), is dominated by circumstellar emission that closely traces optical starlight.

However, the huge scatter seen in the  $70\mu\text{m}$ -Bband panels in Figures 2 and 3 suggest that this colder dust is unassociated with stars and is truly interstellar. The absence of any clear correlation between FIR and optical emission from ellipticals has been discussed by Forbes

(1991), Goudfrooij & de Jong (1995), Trinchieri & Goudfrooij (2002) and Temi et al. (2004). In principle cold, FIR-emitting dust could either be diffusely distributed in the hot gas or confined to dense central clouds similar to those visible in optical absorption (e.g. Lauer et al. 2005). We discuss below our preference for the diffuse component in producing most of the FIR-emission.

It is remarkable that  $L_{70}$  and  $L_{160}$  range over more than two orders of magnitude for galaxies with similar  $L_B$  – this is a significant new result that must be explained. In our previous survey of archival data from *Infrared Space Observatory* (ISO) we found a similar spread in FIR luminosities at 60- $200\mu\text{m}$ , but the FIR luminosities in the ISO data spanned only one order of magnitude for fixed  $L_B$  (Temi et al. 2004). At the time we attributed much of this scatter to the unusual nature of the ISO sample which contained many (post-merger) elliptical galaxies with massive disks of cold, dusty gas. Now with this *Spitzer* sample of (mostly) normal elliptical galaxies we find that the range of FIR luminosities is even larger, although we show in Appendix A that some of the FIR-brightest sample galaxies cannot be regarded as normal. In Figure 4 we show that there is no obvious trend of dust color  $F_{70}/F_{160}$  (i.e. mean dust temperature) with  $L_{70}$  except perhaps a tendency for cooler dust in more FIR-luminous galaxies. A similar conclusion results if we replace  $F_{70}$  on the horizontal axis with  $F_{160}$ ,  $L_{70}$  or  $L_{160}$ .

Figures 5 and 6 show no discernable correlation of either  $L_{70}/L_B$  or  $L_{160}/L_B$  with stellar Balmer line ages or metallicity. However,  $L_{24}/L_B$  may show a slight tendency to decrease with age

$$\log L_{24}/L_B = (30.35 \pm 0.05) - (0.021 \pm 0.005)\text{age} \quad (3)$$

or increase with metallicity

$$\log L_{24}/L_B = (29.95 \pm 0.06) + (0.7 \pm 0.2) \log[Z/H]. \quad (4)$$

A negative correlation of  $L_{24}/L_B$  with age would be expected since the rate of mass loss from evolving stars decreases with stellar age (Piovan et al. 2003), although this expected trend is not supported by our study of elliptical galaxies at mid-IR wavelengths (Temi et al. 2005). It must be noted however that Balmer line ages for the same galaxy often show considerable variation when determined by different authors, so the anticorrelation of  $L_{24}/L_B$  with age needs further confirmation. A positive correlation of  $L_{24}/L_B$  with metallicity in Figure 6 is expected if more interstellar grains are produced by mass-losing stars of higher metallicity. However, this is inconsistent with the negative correlation at  $70\mu\text{m}$  in Figure 6,

$$\log L_{70}/L_B = (30.7 \pm 0.1) - (1.9 \pm 0.4) \log[Z/H]. \quad (5)$$

No correlations with X-ray luminosity with any of the FIR luminosities are visible in Figure 7. Decreasing FIR luminosities with increasing hot gas density might be expected since interstellar grains are destroyed by sputtering which is proportional to the density of the hot gas. However, the relationship between  $L_x$  and gas density is unclear. For example, there is no correlation between  $L_x$  and the hot gas density at  $\sim 10$  kpc in the elliptical galaxies observed with *Chandra* by Humphrey et al. (2006). This disconnect between gas density and  $L_x$  may

arise because the hot gas density on kpc-galactic scales is influenced by intermittent energy supplied by the central black holes, while  $L_x$  is largely determined by more extensive gas that fills the dark halos that surround the elliptical galaxies (Mathews et al. 2006). Consequently, the absence of correlations in Figure 7 is not surprising. Finally, we note that all qualitative features in Figure 7 are preserved if luminosities are replaced with fluxes.

In Figure 8 we compare FIR fluxes with optical emission line fluxes determined by three different observers: Goudfrooij et al. (1994a,b), Macchetto et al. (1996) and Sarzi et al. (2006). The optical observations require difficult background subtraction and the procedures used vary among the observers. For this reason, we compare FIR fluxes in Figure 8 with each set of optical emission line fluxes independently.

We believe that both  $F_{60}$  and  $F_{170}$  correlate weakly with observed optical line fluxes, but that  $F_{24}$  does not. The recent SAURON data for  $F_{H\beta}$  (Sarzi et al. 2006) show the tightest relationship. The Goudfrooij et al. data (left column of panels in Figure 8) are marginally correlated, but the significance increases if it is combined with the Macchetto et al. data (shown in the central column).

In Figure 9 we compare the fluxes in the optical emission lines with B-band fluxes, using only data for non-peculiar E or E/S0 galaxies, excluding peculiar and known S0 galaxies. The top and bottom panels from Macchetto et al. (1996) and Sarzi et al. (2006) show that the line flux is weakly correlated with the stellar continuum (see also Phillips et al. 1986; Macchetto et al. 1996; Goudfrooij 1999). A correlation between extended line emission and the optical continuum suggests that the warm gas with  $T \sim 104$  K has a stellar origin. But the quality of these difficult optical observations is poor. There are very few objects in common among the Goudfrooij, Macchetto and Sarzi data sets, but the flux-flux plots of these common galaxies show large scatter with almost no clear monotonic relationship. Five of the six galaxies in common between Goudfrooij and Macchetto correlate *negatively* in a flux-flux plot.

The correlation in Figure 9, if real, may simply indicate that the warm gas and the dust associated with it both have a stellar origin – more stars of a similar age and metallicity eject more gas. However, the optical emission line flux depends sensitively on the density of the warm gas and therefore on the pressure in the local hot interstellar gas. At present there are too few accurate observations to interpret Figure 9 with confidence.

All ellipticals in our sample show evidence of extended emission at  $24\mu\text{m}$  similar to that of the optical stellar images – details of this will be discussed in a separate publication. However, spatial extension is also evident at  $70\mu\text{m}$  as shown in Table 1, but the emission at  $160\mu\text{m}$  is not spatially resolved due to decreasing resolution at larger wavelengths. Figure 10 shows the surface brightness at  $70\mu\text{m}$  for eight galaxies together with the point response function (PRF) for the MIPS detector (including the first Airy ring). All contours in Figure 10 are arbitrarily normalized to 50 at the center. The (logarithmic) extension in arcseconds beyond the PRF is best measured at 0.08 of the central fluxes, shown with arrows in Figure 10. The full width at  $4/50 = 0.08$  maximum (subsequently referred to as FW0.1M; last two columns

in Table 1) of the PRF is  $37''$ . Twelve galaxies in our full sample have FW0.1M greater than  $40''$ , indicating that these galaxies are spatially resolved at  $70\mu\text{m}$ . When FW0.1M/ $2R_e$  is plotted against  $F_{70}/F_{160}$ , there is no clear evidence that galaxies with more extended  $F_{70}$  have colder dust.

## 5. A SIMPLE FAR-INFRARED SPECTRAL ENERGY DISTRIBUTION

We estimate the FIR spectral energy distribution (SED) from diffusely distributed interstellar dust in elliptical galaxies using a simple model similar to that described in Temi et al. (2003). For completeness and clarity, we briefly describe this model again here. We assume that dust grains ejected from evolving stars come into direct contact with the hot interstellar gas after a short time,  $\lesssim 10^5 - 10^6$  yr, when the stellar gas has heated to the (virial) temperature of the hot interstellar gas. This time scale is established by comparing typical Balmer emission line observations with the luminosity expected if all the gas expelled from stars (at the expected rate for an old stellar population) is ionized and in hydrostatic equilibrium with the hot gas (Mathews & Brighenti 1999). After  $\sim 10^6$  yrs this warm gas at  $10^4$  K must merge with the hot gas since otherwise its Balmer line luminosity would exceed typically observed values. However, the dust in this gas can resist sputtering destruction in the hot interstellar gas ( $T \sim 10^6 - 10^7$  K) for much longer times,  $\sim 10^8$  yrs. Consequently, we model “recently” produced dust that was created by local stars during the previous  $\sim 10^8$  yrs. Once in contact with the hot gas, the dust grains are destroyed by sputtering at a rate

$$\frac{da}{dt} = -3.2 \times 10^{-14} n_p [1 + (2 \times 10^6 / T)^{2.5}]^{-1} \mu\text{m s}^{-1}, \quad (6)$$

where  $a$  is the grain radius (in  $\mu\text{m}$ ) and  $n_p$  is the proton density in the hot gas (Draine & Salpeter 1979; Tsai & Mathews 1995).

If  $N(r, a, t)da$  be the number of grains  $\text{cm}^{-3}$  with radius between  $a$  and  $a + da$  at galactic radius  $r$  at time  $t$ , the grain population evolves according to

$$\frac{\partial}{\partial a} \left[ N \left( \frac{da}{dt} \right) \right] = S(r, a), \quad (7)$$

where  $S(r, a)da$  is the rate at which grains with radii  $a$  are expelled from stars per  $\text{cm}^3$  (Tsai & Mathews 1995). We assume  $S(a) = S_o a^{-s}$  for  $0 < a < a_{\text{max}}$ , with  $s = 3.5$  (Mathis et al. 1977), so the coefficient

$$S_o(r) = \frac{3\delta\alpha_*\rho_*}{4\pi\rho_g 10^{-12}} \frac{(4-s)}{a_{\text{max}}^{4-s}} \quad (8)$$

depends on the rate that the old stellar population ejects mass  $\alpha_* = M_*^{-1} |dM_*/dt| \approx 4.7 \times 10^{-20} \text{ s}^{-1}$  (Mathews, 1989), the stellar density  $\rho_*$ , the initial dust to gas mass ratio scaled to the stellar metal abundance in solar units  $\delta = (1/150)z(r)$ , and the density of (amorphous) silicate grains,  $\rho_g = 3.3 \text{ gm cm}^{-3}$ . The solution of eq. (7) is

$$N(r, a) = \left| \frac{da}{dt} \right|^{-1} \frac{S_o(r)}{(s-1)} a^{1-s} \quad a \leq a_{\text{max}}. \quad (9)$$

The grain temperature  $T_d$  is determined by the balance

of heating (by both absorption of stellar radiation and by electron-grain collisions) and radiative cooling:

$$\int_0^\infty 4\pi J_*(r, \lambda) Q_{abs}(a, \lambda) \pi a^2 d\lambda + 4\pi a^2 \frac{1}{4} n_e \langle v_e E_e \rangle \tau(a) \\ = 4\pi a^2 \sigma_{SB} T_d(r, a)^4 \langle Q_{abs} \rangle(T_d, a). \quad (10)$$

In view of the high electron-grain collision frequency, we neglect stochastic heating due to single impacts.

We assume that all grains have properties similar to astronomical silicates (Laor & Draine 1993) using the following approximations for the absorption coefficient  $Q_{abs} \approx a\psi(\lambda)$ , and for the Planck-averaged values  $\langle Q_{abs} \rangle \approx 1.35 \times 10^{-5} T_d^2 a$  (see Draine & Lee 1984). The mean intensity of starlight is found by integrating over a de Vaucouleurs stellar profile using the appropriate effective radius  $R_e$  and stellar luminosity for each galaxy. The collisional heating term in the equation above includes a correction  $\tau(a)$  for small grains that do not completely stop the incident thermal electrons (Dwek 1986) and  $\langle v_e E_e \rangle = (32/\pi m_e)^{1/2} (kT)^{3/2}$  is an average over a Maxwellian distribution. The electron density and temperature of the hot gas are calculated using deconvoluted profiles from X-ray observations. The FIR emissivity at each wavelength is calculated from

$$j(r, \lambda) = \frac{1}{4\pi} \int_0^{a_{max}} N(r, a) 4\pi a^2 10^{-8} Q_{abs}(a, \lambda) \\ \times \pi B(T_d(r, a), \lambda) da. \quad (11)$$

In Figure 11 we compare the expected FIR spectral energy distribution for three galaxies in our sample that have well-known hot gas density and temperature profiles from X-ray observations: NGC 1399, 1404 and 4472. None of these galaxies are spatially resolved at  $70\mu\text{m}$ . The X-ray data for these galaxies has been taken from the following sources: NGC 1404 & 1399: (Paolillo et al 2002; Jones et al. 1997); NGC 4472: (Mathews & Brighenti 2003; Brighenti & Mathews 1997). The profiles in Figure 11 show the expected FIR spectral energy distributions computed with the equations above. The solid and dashed lines correspond respectively to emission from grains with original maximum sizes  $a_{max} = 0.3\mu\text{m}$  and  $1.0\mu\text{m}$ . The observed fluxes for NGC 1399 and NGC 4472 at  $70\mu\text{m}$  and  $160\mu\text{m}$  are in excellent agreement with our simple model. The fit to NGC 1404 is also satisfactory, given the many assumptions in our model. While the flux at  $24\mu\text{m}$  is also shown in Figure 11, this circumstellar emission is not included in our model, but it supports our assumption that much of the diffuse interstellar dust in these three galaxies has a stellar origin.

It is of particular interest to determine FIR spectral energy distributions for galaxies that have accurate interstellar gas density and temperature profiles and are also spatially resolved at  $70\mu\text{m}$ . Seven galaxies in Table 1 have FW0.1M greater than  $50''$  but only six of these are in the Ellis and O'Sullivan (2006) list of X-ray galaxies detected with ROSAT: NGC 2768, 2974, 4125, 4636, 4696, and 5044. Of these six galaxies, only three – NGC 4636, 4696 and 5044 – have X-ray luminosities ( $\log L_x \gtrsim 41.5$ ) large enough for an accurate determination of the gas density and temperature profiles. However, the optically peculiar elliptical NGC 4696 is the

central galaxy in the Centaurus Cluster with powerful FRI-type radio emission, a large mass of dusty neutral gas and highly disturbed hot cluster gas (Fabian et al. 2006). In view of these complexities, NGC 4696 is an inappropriate galaxy to learn about the nature of FIR emission from normal elliptical galaxies. We find that the observed fluxes for the two remaining FIR-extended galaxies – NGC 5044 and NGC 4636 – are very much larger than predicted by our steady state model for the FIR spectral energy distribution. We believe that the dust in these galaxies has an entirely different origin. The large and extended FIR emission from NGC 5044 and NGC 4636, which is related to the enormous range of FIR luminosities in Figure 3, will be discussed in a separate forthcoming publication.

## 6. DISCUSSION

### 6.1. Large Range of $L_{FIR}$

The first important conclusion to be drawn from Figures 2 and 3 is that warm circumstellar dust and colder interstellar dust behave very differently. The relatively small scatter in  $F_{24}$  in Figure 2 is slightly larger than our estimated observational errors. Nevertheless, we have been unable to find correlations between stellar age or metallicity and the residuals in  $F_{24}$  from the mean correlation. We conclude that the warm dust emitting at  $24\mu\text{m}$  is largely circumstellar and this is confirmed by the similarity of optical and  $24\mu\text{m}$  surface brightness profiles which will be discussed in detail elsewhere.

The second and most remarkable result in Figures 2 and 3 is that the emission from colder dust at 70 and  $160\mu\text{m}$  varies by a huge factor relative to that at  $24\mu\text{m}$  and optical wavelengths. In the previous section and in Figure 11 we show that 70 and  $160\mu\text{m}$  fluxes from three galaxies having well-observed interstellar gas density profiles can be fit reasonably well with our simple dust heating model without varying any of the dust parameters from those we assumed at the outset.

However, notice that all three galaxies in Figure 11 that agree with our model SED – NGC 1399, 1404 and 4472 – have values of  $L_{70}$  and  $L_{160}$  in Table 2 that lie near the bottom of the observed distributions in Figure 3. We think it is impossible to explain the huge dispersion of  $L_{70}$  and  $L_{160}$  in Figure 3 by simply varying the dust parameters in the SED models used for the three galaxies in Figure 11, i.e., the stellar mass loss rate, dust composition, dust size distribution, etc. are unlikely to be in error by an order of magnitude or more. Our SED model clearly fails to fit most of the FIR observations.

Some of the large spread of  $L_{70}$  and  $L_{160}$  in Figure 3 can be understood because our sample includes very FIR-luminous elliptical galaxies that contain abnormal masses of interstellar dust and cold gas, probably acquired by a recent merger. In Appendix A we review relevant observations of 12 sample galaxies having the highest  $70\mu\text{m}$  luminosities in order of descending  $L_{70}$ . We conclude from this limited information that most ellipticals with the largest  $L_{70}$  and  $L_{160}$  in Figure 3 cannot be regarded as typical or normal. Of the 12 galaxies in Appendix A, we regard the following 8 as either likely S0s (which often have extended, rotationally supported, star-forming disks of cold dusty gas) or having massive HI or molecular lanes or disks probably acquired by mergers:

IC 3370, NGC 5018, 2974, 4125, 5322, 2768, 3962, and 5077. These atypical or mis-classified elliptical galaxies are the brightest galaxies in our sample. However, we regard the following galaxies in Appendix A with slightly lower  $L_{70}$  as normal or quasi-normal ellipticals: NGC 3557, 5044, 4589, and (possibly) 4697. If we disregard the eight galaxies with atypical dust content, the range in  $L_{70}$  and  $L_{160}$  occupied by normal ellipticals is reduced from  $\sim 100$  (shown in Figure 3) to about  $\sim 30$ , but this is still larger than can be explained by varying dust parameters in our SED model. These normal ellipticals with excess FIR are the most interesting galaxies in our sample.

### 6.2. Location of FIR-Emitting Dust

We assume that galaxies with  $L_{FIR}$  significantly above that predicted by our model SEDs in Figure 11 have dust contents that exceed those that can be understood by a steady state balance between dust creation by mass-losing stars and dust destruction by sputtering. Galaxies in Figure 3 with  $\log L_{70} \gtrsim 40.5$  must contain additional cold dust from another source. This additional cold dust is either (1) spread diffusely throughout a large region of the galactic hot interstellar gas or (2) located in dense optically thick clouds similar to those seen in absorption by optical observers. In Appendix B we describe a simple argument that supports the first option above, diffuse FIR emission. We suppose in Appendix B that the FIR-emitting dust is in a small spherical cloud of radius  $r_c$  located at the center of an elliptical galaxy. The dust is heated both by internal stars and by starlight incident from the entire galaxy. The dust cloud is assumed to be optically thick to most stellar radiation. As the cloud radius  $r_c$  is increased, the estimated  $70\mu\text{m}$  luminosity also increases because the cloud encloses more stars and intercepts more light from external stars. However, this simple dusty cloud model cannot account for the luminosity range in Figure 3 unless  $r_c$  is so large ( $\gtrsim 200$  pc) that it would be easily apparent in moderate resolution optical images. The UV-ionized surfaces of these clouds may also be visible. While AGN heating within optically thick dusty clouds could easily provide the needed FIR energy, this seems unlikely since AGNs would need to be bolometrically brighter than the stars within  $r_c$  and would therefore be seen in those ellipticals in which the dusty clouds are in disks or not present at all. Such luminous AGN would almost certainly be visible at other frequencies.

Comparisons of the most FIR-luminous (normal) ellipticals in our sample with recent HST images (e.g. van Dokkum & Franx 1995; Lauer et al. 2005), show a correspondence between the absence of nuclear dust and low  $L_{FIR}$ . For example, of the 19 galaxies in common between our sample and that of Lauer et al. (2005), all 11 of the ellipticals with  $L_{70} > 10^{40.5}$  erg s $^{-1}$  have detectable nuclear dust, while all but one of the 9 galaxies with  $L_{70} < 10^{40.5}$  have no nuclear dust detected. Nevertheless, even for these galaxies with lower  $L_{70}$  we believe that most of the  $L_{FIR}$  comes from a diffuse component. In addition to the argument in Appendix B, our preference for extended excess dust is supported by noting that all six galaxies with extended FIR emission in Table 1 (e.g. FW0.1M  $> 50''$ ) have excess FIR emission, i.e.

$$L_{70} > 10^{40.5} \text{ erg s}^{-1}.$$

### 6.3. External Origin for the Excess Dust

If the FIR emission in excess of that expected from our simple model SED in Figure 11 is from cold dust diffusely distributed throughout the hot interstellar gas, where has it come from? It is often supposed that optically-observed dust in elliptical galaxies has an external origin, resulting from a recent merger with a small dust-rich galaxy that is otherwise difficult to observe. We adopted this explanation previously in our discussion of the excess dust in NGC 4636 (Temi, et al. 2003), which we interpreted as a dusty merger that occurred within the last  $\sim 3 \times 10^8$  yrs, the estimated sputtering time in the hot gas in this galaxy. However, it has since been determined that the mean stellar age in NGC 4636 is very old (10.3 Gyrs, Sanchez-Blazquez et al. 2006), and this strongly argues against a merger  $\sim 3 \times 10^8$  yrs ago with a dusty, star-forming galaxy. Moreover, we observe that the additional dust in NGC 4636 is extended (FW0.1M =  $54.4''$  in Table 1) and appears to be distributed rather evenly about the center unlike the irregular distribution that might be expected to result from a recent merger undergoing dynamical friction with accompanying ram-stripping and tidal disruption. So our previous interpretation of NGC 4636 needs to be reevaluated.

The dust sputtering time for grains of initial radius  $a$  in the hot gas of an elliptical galaxy is  $t_{sp} \approx a/|da/dt|_{sput} \approx 1.2 \times 10^8 a_{\mu} (n_e/10^{-2})^{-1}$  yrs (where  $a_{\mu}$  is in microns) provided the ambient gas temperature is  $T \gtrsim 10^6$  K. (Draine & Salpeter 1979; Tsai & Mathews 1995). Even if the dust is mixed with warm gas at  $T \sim 10^4$  K, where sputtering is negligible, its overall sputtering destruction time  $t_{sp}$  cannot be significantly reduced since, as discussed below, we generally expect that the warm gas is thermally heated and joins the (spatially extended) hot gas phase on a time scale  $\sim 10^6$  yrs that is very much less than  $t_{sp}$ . Therefore it is reasonable to assume that the diffuse FIR-emitting dust in our sample galaxies is in direct contact with the hot gas during most of its sputtering lifetime.

The dynamical (freefall) time of a merging dusty galaxy across the optical image of a large elliptical is several  $\sim 10^8$  years, comparable to  $t_{sp}$ . Therefore, on the merger hypothesis, diffusely distributed cold dust must be resupplied by mergers in a regular fashion at least every  $\sim 10^8$  yrs. Therefore, an entourage of dusty merging galaxies should be commonly observed in the outer regions of the majority of elliptical galaxies having FIR excess emission – but they are not. In fact, mergers between elliptical and (small) dust rich galaxies are rarely observed at zero redshift. While we believe that mergers do occur and that some of the most FIR luminous galaxies in our sample can only be explained by mergers, the similarity of the sputtering and dynamical time scales makes it difficult to accept the proposition that mergers are the dominant or only source of (extended) dust in most luminous elliptical galaxies. This point of view is supported by Figure 5, showing that the incidence of young stars in elliptical galaxies is uncorrelated with the FIR excess luminosities seen in Figure 3.

### 6.4. Internal Origin for Excess Dust

#### 6.4.1. Evolution of Dust Ejected from Stars

Before exploring the origin of the additional dust required to produce FIR luminosities in excess of  $L_{70} \sim 10^{40.5} \text{ erg s}^{-1}$ , it is useful to review the evolution of cold dusty gas that is introduced into the hot, X-ray emitting interstellar gas by mass-losing red giant stars. Our SED model is based on an internal stellar source of dust which is confirmed by mid-IR observations of (apparently out-flowing) circumstellar dust (Knapp et al. 1989; Athey et al. 2002; Bressan et al. 2006; Bregman et al. 2006). We think that the fate of this dusty gas varies with galactic radius.

Throughout most of the volume occupied by galactic stars beyond  $\sim 1$  kpc, we assume that both the dust and gas ejected from red giant stars ultimately merge with the hot gas which is the dominant interstellar phase. We expect that gas recently ejected from stars can be maintained in pressure equilibrium at warm temperatures ( $T \approx 10^4$  K) by photoionization by UV emitted by post-AGB stars. Emission from warm gas at  $r \gg 1$  kpc is faint and has not been observed. Eventually this warm gas thermally mixes with nearby hot gas. When the dust in this gas confronts the hot gas it will be destroyed by sputtering in  $\sim 10^8$  yrs.

However, within  $\sim 1$  kpc of the centers of elliptical galaxies the evolution of dusty stellar ejecta is different. Extended warm gas in this region is commonly observed, but its velocities differ from those of nearby stars (e.g. Caon, Macchetto & Pastoriza 2000). Evidently the hot and warm gas exchanged momentum when the warm gas had a much lower density. After dusty stellar envelopes and winds are ejected from orbiting red giant stars, the gas expands until its density approaches (but still exceeds) the local hot gas density. At this time the ejected gas, which is still moving with the stellar orbital velocity, is disrupted by hydrodynamic instabilities and shocked to a few million degrees where its density is comparable to that of the hot interstellar gas. During this period of interaction between the stellar ejecta and the hot gas, momentum is exchanged and the ejected gas acquires some of the velocity of the ambient hot gas. Even if the gas ejected from stars is (transiently) heated completely to the temperature of the local hot gas ( $\sim 10^7$  K), its dust content will cool the gas rapidly back to  $\sim 10^4$  where it is stabilized by UV from post-AGB stars. This rapid dust-assisted cooling occurs because of very frequent inelastic collisions between thermal electrons in the hot gas and the dust grains. Mathews & Brighenti (2003) showed that efficient dust cooling of the hot gas is also faster than the sputtering lifetime of the dust, so the gas retains some dust after it cools to  $\sim 10^4$  K. Since the cooling time to  $\sim 10^4$  K within 1 kpc is less than the dynamical time in the local (stellar) potential, these dense warm clouds freefall toward the galactic center and accumulate there. As dusty warm gas collects into a disk near the center, similar to those observed by van Dokkum & Franx (1995) and Lauer et al. (2005), it eventually becomes optically thick to the stellar UV radiation. Because of its residual dust, we expect molecular formation and eventual cooling far below  $10^4$  K. Dense, cold nuclear dust disks and clouds similar to those observed can form naturally from stellar mass loss in elliptical galaxy cores (Mathews & Brighenti 2003). Dusty galaxy mergers are not required. We speculate below that this central dust reservoir may

be the source of extended diffuse FIR emission in many ellipticals.

Central dusty clouds and disks in ellipticals are not merely an amusing curiosity, but are likely to be key to understanding the energetics of AGN feedback in regulating cooling flows in the hot gas within and around elliptical galaxies. Indeed, Simoes Lopes et al. (2006) find a correlation between nuclear dust and AGN activity in elliptical galaxies. Consider the black hole accretion luminosity expected in a large group-centered elliptical galaxy by dusty mass loss just within the central kpc where rapid dust-assisted cooling is expected. Accretion is expected to quickly follow cooling. The AGN luminosity is  $L_{agn} = \epsilon \dot{M} c^2 = 6 \times 10^{45} [\dot{M}_1 / (M_\odot \text{ yr}^{-1})] (\epsilon / 0.1) \text{ erg yr}^{-1}$  where  $\dot{M}_1$  is the total rate of stellar mass loss within the central kpc. Since a  $10^{10}$  year old stellar population of mass  $M_*$  ejects  $1.5(M_*/10^{12} M_\odot) M_\odot \text{ yr}^{-1}$ , the stellar mass within 1 kpc,  $\sim 5 \times 10^{10} M_\odot$ , generates  $\dot{M}_1 \approx 0.07 M_\odot \text{ yr}^{-1}$ . When accreted by the central massive black hole, this translates into a luminosity  $L_{agn} \approx 4 \times 10^{44} \text{ ergs s}^{-1}$  that exceeds the entire X-ray luminosity of the most luminous galaxy groups,  $L_x \sim 3 \times 10^{43} \text{ ergs s}^{-1}$ . Consequently, dusty stellar mass loss within the central kpc of bright ellipticals can generate enough accretion energy to balance the entire bolometric X-ray luminosity of a large galaxy group. The heating of the hot gas as a consequence of this accretion also provides enough energy to drive buoyant mass circulation in the hot gas out to 5-10 kpc.

The evolution of dusty disks in galactic cores that we just described cannot continue very long. If small core disks accrete dusty gas at  $\dot{M}_1 \approx 0.07 M_\odot \text{ yr}^{-1}$ , for  $\sim 10^{10}$  yrs, and allowing for a larger mass-loss rate in the past, currently observed disks should have a typical mass of  $\sim 10^{10} M_\odot$  and a dust mass of  $\sim 10^8$ , both far in excess of those observed. (Small stellar disks with masses  $\sim 10^9 - 10^{10} M_\odot$  are not commonly observed in the cores of most ellipticals, so normal star-formation is ruled out.) A large minority of bright ellipticals show no evidence of central dusty disks/clouds. Where has this dusty gas gone?

#### 6.4.2. Explosive Ejection of Dust from the Galactic Core

The excess diffuse dust observed in FIR-emission may have been exploded out from the centers of elliptical galaxies by the release of AGN energy. We estimate from our model SED that the total mass of excess dust required to explain the FIR luminosities in Figure 3 is  $M_d \sim 3 \times 10^5 M_\odot$ . This is comparable to the estimated dust masses in the central dusty disks or lanes (e.g. Goudfrooij & de Jong 1995). If the (very uncertain) dust to gas mass ratio is  $\delta \approx 0.01$ , then the mass of gas that initially contained this dust is  $M \sim 10^7 - 10^8 M_\odot$ . If cold dusty gas is ballistically ejected from the core out to a few kpc, velocities of  $\sim 100 \text{ km s}^{-1}$  are required. The kinetic energy needed to explosively transport dusty gas from the galactic core to  $\sim 1$  kpc is  $E_k \approx 0.5 M v^2 = 10^{55} (0.01/\delta) (M_d/10^6 M_\odot) (v/100 \text{ km/s})^2 \text{ ergs}$ . Although very uncertain, the energy involved is certainly larger than that of a single supernova. Since multiple starburst activity in elliptical galaxies is very rare, AGN energy is required for dust ejection from the core. If the AGN dust ejection process is intermittent, this would

explain those elliptical galaxies that are not observed to have optically obscuring dust in their cores or extended FIR excess emission. The FIR variance expected from intermittent AGN outbursts obviates the argument of Forbes (1991) and Simoes Lopes et al. (2006) that the failure of an  $L_{FIR}$ - $L_B$  correlation necessarily requires an external source of dust by mergers. Some explosive character to the AGN-dust cloud interaction is implied by the chaotic nature of the central dust observed in many HST images (Lauer et al. 2005). This chaotic, denser dusty gas is highly transient and must have been ejected from the core. These chaotic clouds cannot be understood as infalling stellar ejecta (as suggested by Lauer et al.), formed by the coalescence of many dusty stellar envelopes produced by individual stars, since the free fall time ( $\sim 10^6$  yrs) to the galaxy center is too short for such accumulations to occur.

However, explosive ejections of central dust to  $\sim 5-10$  kpc with energies  $E_k \gtrsim 10^{55}$  ergs would produce kpc-sized central cavities, strong shocks and heated cores that are rarely observed in X-ray images while extended excess FIR emission is common. This may be the best argument against explosive dust transport.

#### 6.4.3. Buoyant Ejection of Dust from the Galactic Core

Density irregularities and multi-temperature X-ray spectra of the hot interstellar gas in elliptical galaxies reveal buoyant activity, presumably related to a less explosive heating of the hot gas with AGN energy (Buote, Lewis, Brighenti & Mathews 2003a,b). In view of these X-ray observations, it is plausible that central dust can be buoyantly transported out to  $\sim 5-10$  kpc, producing the extended FIR emission that we observe.

The buoyant rise time  $t_{buoy}$  of heated gas is expected to be comparable to or somewhat less than the sputtering destruction time in the buoyant gas. For example in the galaxy/group NGC 5044 the freefall time from radius  $r_{kpc}$  to the galactic center is  $t_{ff} = 4.5 \times 10^6 r_{kpc}^{0.87}$  yrs, based on a mass model that combines a de Vaucouleurs stellar profile ( $M_* = 3.37 \times 10^{11} M_\odot$ ;  $r_e = 10$  kpc) with an Navarro-Frenk-White dark halo (mass  $M_{halo} = 4 \times 10^{13} M_\odot$ ; concentration  $c = 8.67$ ). The buoyancy rise time  $t_{buoy} = \beta t_{ff}$  is greater than  $t_{ff}$  by some factor  $\beta \gtrsim 1$ . From Draine & Salpeter (1979) the approximate grain sputtering time is  $t_{sput} \approx 2.4 \times 10^6 a_\mu n_e(r)^{-1}$  where  $a_\mu$  is the grain radius in microns. Adopting  $n_e \approx 0.085 r_{kpc}^{-0.87} \text{ cm}^{-3}$  for the observed hot gas density in NGC 5044 within 30 kpc, the local sputtering time is nearly proportional to  $t_{ff}$ ,  $t_{sput} \approx 1.8 a_\mu t_{ff}$ . However, the buoyant gas will have a density that is  $\delta < 1$  times lower than the observed hot gas density. Therefore, we see that the ratio of the local sputtering time in the buoyant gas to the buoyancy rise time is  $\sim 1.8 a_\mu / (\delta \beta)$ , which may well exceed unity considering the many uncertainties involved.

The exact nature of the AGN energy release that initiates buoyant activity is unclear at present. In about half of the ellipticals with optically visible dust, the images of the obscuring dust are morphologically ‘‘chaotic’’ and distributed in an asymmetric fashion away from the center of the galaxy (Lauer et al. 2005). Evidently the AGN energy is sufficient to disrupt the dense central dusty disks and lanes which must reform again later by local

stellar mass loss. It is interesting that the radii of the dusty disks observed by Lauer et al. (2005) do not correlate with the stellar rotation, also suggesting short disk lifetimes and intermittent disruption of the dusty disks.

Regardless of the mode of outward dust transport, explosive or buoyant, when the dust rises to 5-10 kpc it may cause the hot gas to cool back to warm gas temperatures  $\sim 10^4$  K. The correlations in Figure 8 between  $F_{70}$  and  $F_{160}$  and the optical line fluxes, if real, indicate a connection between the warm gas and (excess) dust. Similar morphologies of gas and dust images have been discussed by optical observers (e.g. Goudfrooij et al. 1994). Although optical line fluxes appear to correlate with the FIR and B-band fluxes, Figure 2 shows that the FIR and B-band fluxes do not mutually correlate. This can be understood if most of the FIR-emitting dust comes not from recent stellar mass loss, but is transported out from a reservoir in the galactic core, which contains a large mass of dust unrelated to the the global stellar B-band flux or luminosity.

## 7. CONCLUSIONS

Our main conclusions are:

- (1) The optical luminosities  $L_B$  of elliptical galaxies correlate with luminosities at  $24\mu\text{m}$  ( $L_{24}$ ) but not with  $L_{70}$  or  $L_{160}$ . This indicates that the transition between circumstellar and interstellar dust occurs for dust grains with emission that peaks somewhere between  $24\mu$  and  $70\mu\text{m}$ .
- (2) Elliptical galaxies with similar  $L_B$  have  $L_{70}$  and  $L_{160}$  that vary over a factor  $\sim 100$ . This variation is reduced to  $\sim 30$  if abnormally dust-rich ellipticals are excluded from the sample.
- (3) Neither  $L_{70}/L_B$  nor  $L_{160}/L_B$  correlates with the stellar age or metallicity of the galaxies.
- (4) Weak correlations appear between optical line emission fluxes from warm ( $\sim 10^4$  K) gas and  $F_{70}$  and  $F_{160}$ . This suggests a relationship between dust and gas that may have cooled from the hot phase.
- (5) Seven galaxies in our sample are clearly extended at  $70\mu$  with FW0.1M exceeding  $50''$  corresponding to 5–10 kpc.
- (6) The luminosities and spectral energy distributions of elliptical galaxies with the lowest  $L_{70}$  and  $L_{160}$  are consistent with a simple steady state dust model in which dust expelled from stars is eroded by sputtering in the hot interstellar gas.
- (7) We show in Appendix B that the observed emission at 70 and  $160\mu\text{m}$  cannot come from small optically visible clouds in the galactic cores similar to those seen in HST images.
- (8) In view of the common occurrence of spatially extended emission at  $70\mu\text{m}$  in many ellipticals, it is unlikely that this dust can be supplied by successive mergers with gas-rich galaxies, each occurring during the relatively short sputtering lifetime of the diffuse dust,  $\sim 10^8$  yrs. Additional supporting evidence for such mergers is lacking.



(9) The appearance of extended FIR-emitting dust in otherwise normal elliptical galaxies can be understood by the disruption and buoyant transport of centrally accumulated dust by intermittent AGN activity. The buoyant rise time out to 5-10 kpc,  $\sim 10^7$  yrs, is less than the sputtering lifetime of the dust,  $\sim 10^8$  yrs.

This work is based on observations made with the Spitzer Space Telescope, which is operated by the Jet

Propulsion Laboratory, California Institute of Technology, under NASA contract 1407. Support for this work was provided by NASA through Spitzer Guest Observer grant RSA 1276023. Studies of the evolution of hot gas in elliptical galaxies at UC Santa Cruz are supported by NASA grants NAG 5-8409 & ATP02-0122-0079 and NSF grant AST-0098351 for which we are very grateful. We thank Justin Harker for his help with the photometric properties of old stellar populations.

## REFERENCES

- Athey, A., Bregman, J. N., Bergman, J. D., Temi, P. & Sauvage, M. 2002, *ApJ*, 571, 272
- Barnes, J. E. & Hernquist, L. 1992, *ARA&A*, 30, 705
- Bell, E. F. et al. 2004, *ApJ*, 608, 752
- Bertola, F., Buson, L. M. & Zeilinger, W. W. 1992, *ApJ*, 410, L79
- Birkinshaw, M. & Davies, R. L. 1985, *ApJ*, 291, 32
- Bregman, J. N., Temi, P. & Bregman, J. D. 2006, 647, 265
- Bressan, G. et al. 2006, *ApJ*, 639, 55
- Brighenti, F. & Mathews, W. G. 1997, *ApJ*, 486, L83
- Buote, D. A., Lewis, A. D., Brighenti, F. & Mathews, W. G. 2003a, *ApJ*, 594, 741
- Buote, D. A., Lewis, A. D., Brighenti, F. & Mathews, W. G. 2003b, *ApJ*, 595, 151
- Buson, L. M. et al. 1993, *A&A*, 280, 409
- Caon, N., Macchetto, D. & Pastoriza, M. 2000, *ApJS* 127, 39
- Carollo, C. M. & Danziger, I. J. 1994, *MNRAS*, 270, 743
- Carollo, C. M., Franx, M., Illingworth, G. D., Forbes, D. A. 1997, *ApJ*, 481, 710
- Dale D. A. et al. 2005, *ApJ*, 633, 857
- Denicolo, G. et al. 2004, *MNRAS*, 358, 813
- Draine, B. T. & Salpeter, E. E. 1979, *ApJ*, 231, 77
- Draine, B. T. & Lee, H. M. 1984, *ApJ*, 285, 89
- Dwek, E. 1986, *ApJ*, 302, 363
- Emsellem, E. et al. 2004, *MNRAS*, 352, 721
- Ellis, S. C. & O'Sullivan, E. 2006, *MNRAS*, 367, 627
- Faber, S. M. 2006, *ApJ* (submitted) (astro-ph/0506044)
- Fabian A. C., Sanders, J. S., Taylor, G. B. & Allen, S. W. 2006, *MNRAS*, (in press) (astro-ph/0503154)
- Fazio, G. G. et al. 2004, *ApJS*, 154, 10
- Ferrari, F., et al. 1999, *A&AS*, 136, 269
- Filho, M. E. et al. 2002, *ApJS*, 142, 223
- Forbes, D. A. 1991, *MNRAS*, 249, 779
- Fried, J. W. & Illingworth, G. D. 1994, *AJ*, 107, 992
- Funes, J. G. et al. 2002, *A&A*, 388, 50
- Goudfrooij, P. 1994, Ph.D. Thesis, University of Amsterdam, The Netherlands
- Goudfrooij, P. et al. 1994a, *A&AS*, 104, 179
- Goudfrooij, P. et al. 1994b, *A&AS*, 105, 341
- Goudfrooij, P. & de Jong, T. 1995 *A&A*, 298, 784
- Goudfrooij, P. 1999, in *Star Formation in Early-Type Galaxies* eds. J. Cepa & P. Carral, ASP Conf. Ser. v. 163, 55
- Humphrey, P. et al. 2006, *ApJ*, 646, 899
- Jarvis, B. J. 1987, IAU Symposium *Structure and Dynamics of Elliptical Galaxies*, ed. T. de Zeeuw, 411
- Jones, et al. 1997, *ApJ*, 482, 143
- Kennicutt, R. C. et al. 2003, *PASP*, 115, 928
- Kim, D.-W. et al. 1988, *ApJ*, 330, 684
- Knapp, G. R., Guhathakurta, P., Kim, D.-W., & Jura, M. A. 1989, *ApJS*, 70, 329
- Koprolin, W. & Zeilinger, W. W. 2000, *A&AS*, 145, 71
- Laor, A. & Draine, B. T. 1993, *ApJ*, 402, 441
- Lauer, T. R. et al. 2005, *AJ*, 129, 2138
- Leonardi, A. J. & Worthey, G. 2000, *ApJ*, 534, 650
- Macchetto, F. et al. 1996, *A&AS*, 120, 463
- Makovoz, D. Roby, T., Khan, I., Booth, H. 2006, *SPIE*, 6274, 10
- Mathews, W. G. et al. 2006, *ApJ*, 652, L17
- Mathews, W. G. 1989, *AJ* 97, 42
- Mathews, W. G. & Brighenti, F. 1999, *ApJ* 526, 114
- Mathews, W. G. & Brighenti, F. 2003, *ApJ* 599, 992
- Mathews, W. G., Brighenti, F. & Buote, D. 2004, *ApJ*, 615, 662
- Mathis, J. S., Ruml, W. & Nordsieck, K. H. 1977, *ApJ*, 217, 425
- Michard, R. 1999, *A&AS*, 137, 245
- Michard, R. 2006, *A&A*, 449, 519
- Mollenhoff, C. & Bender, R. 1989, *A&A*, 214, 61
- Moellenhoff, C., Hummel, E. & Bender, R. 1992, *A&A*, 255, 35
- Naab, T., Jesseit, R. & Burkert, A. 2006, *MNRAS*, 328, 461
- Paolillo et al. 2002, *ApJ*, 565, 883
- Paturel, G., Andernach, H., Bottinelli, L., di Nella, H., et al., 1997, *A&AS*, 124, 109
- Phillips, M. M. et al. 1986, *AJ*, 91, 1062
- Piovan, L., Tantalò, R., Chiosi, C., 2003, *A&A*, 408, 559
- Proctor, R. N. & Sansom, A. E. 2002, *MNRAS*, 333, 517
- Rampazzo, R. et al. 2005, *A&A*, 433, 497
- Richter, O.-G., Sackett, P. D., & Sparke, L. S. 1994, *AJ*, 107, 99
- Rieke, G. H. 2004, *ApJS*, 154, 25
- Samurovic, S. & Danziger, I. J. 2005, *MNRAS*, 363, 769
- Sanchez-Blazquez, P., Gorgas, J., Cardiel, N. & Gonzalez, J.J. 2006, *A&A*, 457, 809
- Sandage, A. & Tamman, G. A., 1981, *Carnegie Inst. of Washington*, Publ. 635
- Sandage, A. & Bedke, J. 1994, *The Carnegie Atlas of Galaxies*, vol 1
- Sarzi, M. et al. 2006, *MNRAS*, 366, 1151
- Shen, S., et al. 2003, *MNRAS*, 343, 978
- Simoes Lopes, R. D., Storchi-Bergmann, T., de Fatima O. Saraiva, M. & Martini, P. 2006, *ApJ* (in press) (astro-ph/0610380)
- Sofue, Y. & Wakamatsu, K. I. 2003, *PASJ*, 45, 529
- Tantalò, R. & Chiosi, C. 2004, *MNRAS*, 353, 405
- Temi, P., Mathews, W. G., Brighenti, F. & Bregman, J. D. 2003, *ApJ*, 585, 121
- Temi, P., Brighenti, F., Mathews, W. G. & Bregman, J. D. 2004, *ApJS*, 151, 237
- Temi, P., Mathews, W. G. & Brighenti, F. 2005, *ApJ*, 622, 235
- Trinchieri, G. & Goudfrooij, P. 2002, *A&A*, 386, 472
- Tsai, J. C. & Mathews, W. G. 1995, *ApJ*, 448, 84
- Tsai, J. C. & Mathews, W. G. 1996, *ApJ*, 468, 571
- van Dokkum, P. G. & Franx, M. 1995, *AJ*, 110, 2027
- Verdoes, Kleijn, G. A., & de Zeeuw, P. T. 2005, *A&A*, 435, 43
- Werner, M. W., et al. 2004, *ApJS*, 154, 1
- Wicklind, T., Combes, F. & Henkel, C. 1995, *A&A*, 297, 643
- Xilouris, E. M. et al. 2004, *A&A*, 416, 41
- Zeilinger, W. W. et al. 1996, *A&AS*, 120, 257

TABLE 1

| Name     | Sample <sup>a</sup> | T <sup>b</sup> | Flux Density        |                     |                      | D <sup>c</sup> | R <sub>e</sub> | 70 $\mu$ m FWHM |       | 70 $\mu$ m FW0.1M |       |
|----------|---------------------|----------------|---------------------|---------------------|----------------------|----------------|----------------|-----------------|-------|-------------------|-------|
|          |                     |                | 24 $\mu$ m<br>(mJy) | 70 $\mu$ m<br>(mJy) | 160 $\mu$ m<br>(mJy) |                |                | ( $''$ )        | (Kpc) | ( $''$ )          | (Kpc) |
| NGC 507  | Temi                | -3.3           | ...                 | < 2.8               | ...                  | 71.99          | 77.1           |                 |       |                   |       |
| NGC 533  | Temi                | -4.8           | 7.1 $\pm$ 3.1       | 23.7 $\pm$ 4.9      | 26.1 $\pm$ 5.6       | 68.23          | 47.5           |                 |       |                   |       |
| NGC 584  | Kennicutt           | -4.6           | 47.6 $\pm$ 7.6      | 49.8 $\pm$ 6.9      | < 17.2               | 23.76          | 27.4           |                 |       |                   |       |
| NGC 596  | Surace              | -4.3           | 15.9 $\pm$ 4.6      | 21.4 $\pm$ 5.1      | 16.7 $\pm$ 7.3       | 23.87          | 30.0           |                 |       |                   |       |
| NGC 636  | Surace              | -4.8           | 10.3 $\pm$ 3.6      | < 16.4              | < 24.5               | 22.28          | 18.9           |                 |       |                   |       |
| NGC 720  | Temi                | -4.8           | 25.6 $\pm$ 5.1      | 18.2 $\pm$ 4.9      | < 21.0               | 22.29          | 39.5           |                 |       |                   |       |
| NGC 855  | Kennicutt           | -4.6           | 72.3 $\pm$ 8.5      | 1335 $\pm$ 36       | 2086 $\pm$ 46        | 9.33           | 18.9           | 22.5            | 1.0   | 58.2              | 7.6   |
| NGC 1377 | Kennicutt           | -2.1           | 1603 $\pm$ 40       | 4988 $\pm$ 71       | 2375 $\pm$ 48        | 22.20          |                |                 |       |                   |       |
| NGC 1395 | Kaneda              | -4.8           | 45.4 $\pm$ 6.5      | 129 $\pm$ 11        | 194 $\pm$ 14         | 21.98          | 45.4           |                 |       |                   |       |
| NGC 1399 | Temi                | -4.5           | 59.9 $\pm$ 7.3      | 15.9 $\pm$ 7.6      | 24.1 $\pm$ 8.6       | 19.40          | 42.4           |                 |       |                   |       |
| NGC 1404 | Kennicutt           | -4.7           | 56.6 $\pm$ 6.3      | 32.6 $\pm$ 6.3      | < 32.2               | 19.40          | 26.7           |                 |       |                   |       |
| NGC 1407 | Kaneda              | -4.5           | 42.5 $\pm$ 6.4      | ...                 | < 35.4               | 22.08          | 71.8           |                 |       |                   |       |
| NGC 1700 | Surace              | -4.7           | 18.7 $\pm$ 4.9      | 29.3 $\pm$ 5.3      | 40.3 $\pm$ 7.2       | 38.04          | 13.7           |                 |       |                   |       |
| NGC 2325 | Temi                | -4.7           | 27.0 $\pm$ 6.4      | 36.5 $\pm$ 6.8      | 21.7 $\pm$ 6.4       | 31.92          | 86.5           |                 |       |                   |       |
| NGC 2768 | Temi                | -4.3           | 46.6 $\pm$ 8.2      | 694 $\pm$ 26        | 377 $\pm$ 29         | 22.38          | 53.5           | 21.4            | 2.3   | 56.4              | 6.1   |
| NGC 2974 | Kaneda              | -4.7           | 62.5 $\pm$ 12.4     | 682 $\pm$ 18        | 1979 $\pm$ 54        | 30.33          | 36.9           | 22.8            | 3.4   | 55.4              | 8.1   |
| NGC 2986 | Temi                | -4.7           | 13.7 $\pm$ 4.8      | < 2.8               | < 14.5               | 32.51          | 41.4           |                 |       |                   |       |
| NGC 3265 | Kennicutt           | -4.8           | 287 $\pm$ 17        | 1952 $\pm$ 44       | 2312 $\pm$ 49        | 21.33          |                |                 |       |                   |       |
| NGC 3379 | Fazio               | -4.8           | 65.5 $\pm$ 8.8      | 60.5 $\pm$ 8.0      | 59.1 $\pm$ 8.2       | 10.71          | 35.2           |                 |       |                   |       |
| NGC 3557 | Temi                | -4.8           | 30.5 $\pm$ 4.5      | 263 $\pm$ 16        | 247 $\pm$ 18         | 34.51          | 37.8           | 20.0            | 3.3   | 38.8              | 6.5   |
| NGC 3610 | Surace              | -4.2           | 18.1 $\pm$ 4.5      | 19.1 $\pm$ 7.3      | 32.8 $\pm$ 16.5      | 29.24          | 12.8           |                 |       |                   |       |
| NGC 3923 | Temi                | -4.6           | 42.9 $\pm$ 6.7      | 22.7 $\pm$ 5.4      | 44.0 $\pm$ 7.8       | 19.14          | 53.3           |                 |       |                   |       |
| NGC 3962 | Kaneda              | -4.7           | 21.5 $\pm$ 5.6      | 374 $\pm$ 18        | 495 $\pm$ 24         | 23.23          | 34.4           | 22.6            | 2.5   | 44.0              | 5.0   |
| NGC 4125 | Kennicutt           | -4.8           | 53.7 $\pm$ 6.9      | 773 $\pm$ 28        | 1395 $\pm$ 37        | 27.79          | 59.9           | 21.6            | 2.9   | 56.8              | 7.7   |
| NGC 4365 | Cote'               | -4.8           | 21.7 $\pm$ 4.7      | 63.8 $\pm$ 8.0      | 52.9 $\pm$ 7.3       | 17.06          | 57.2           |                 |       |                   |       |
| NGC 4472 | Fazio               | -4.8           | 73.3 $\pm$ 8.6      | 58.1 $\pm$ 7.6      | 60.4 $\pm$ 7.8       | 17.06          | 104.0          |                 |       |                   |       |
| NGC 4552 | Kennicutt           | -4.6           | 57.3 $\pm$ 7.8      | 92.1 $\pm$ 10.2     | 171 $\pm$ 16         | 17.06          | 30.0           |                 |       |                   |       |
| NGC 4589 | Kaneda              | -4.8           | 14.9 $\pm$ 4.5      | 262 $\pm$ 16        | 360 $\pm$ 21         | 26.30          | 41.4           | 22.6            | 2.9   | 45.6              | 5.8   |
| NGC 4621 | Cote'               | -4.8           | 34.2 $\pm$ 6.3      | 31.7 $\pm$ 5.7      | 43.4 $\pm$ 6.6       | 17.06          | 46.5           |                 |       |                   |       |
| NGC 4636 | Fazio               | -4.8           | 31.2 $\pm$ 5.6      | 188 $\pm$ 12        | 169 $\pm$ 14         | 17.06          | 101.7          | 22.3            | 1.8   | 54.4              | 4.5   |
| NGC 4649 | Fazio               | -4.6           | 106 $\pm$ 10        | 46.3 $\pm$ 6.8      | < 27.5               | 17.06          | 73.6           |                 |       |                   |       |
| NGC 4660 | Cote'               | -4.7           | 15.2 $\pm$ 4.3      | 36.4 $\pm$ 6.2      | 53.7 $\pm$ 8.2       | 17.06          | 12.8           | 20.0            | 1.7   | 39.0              | 3.2   |
| NGC 4696 | Sparks              | -3.7           | 22.9 $\pm$ 4.7      | 127 $\pm$ 13        | 269 $\pm$ 21         | 39.65          | 212.4          | 22.6            | 4.4   | 52.2              | 10.1  |
| NGC 4697 | Surace              | -4.8           | 43.8 $\pm$ 6.7      | 589 $\pm$ 25        | 755 $\pm$ 28         | 16.22          | 75.3           |                 |       |                   |       |
| NGC 4915 | Surace              | -4.5           | 11.5 $\pm$ 5.5      | 29.2 $\pm$ 4.8      | 54.2 $\pm$ 8.9       | 46.98          | 7.9            |                 |       |                   |       |
| NGC 5018 | Surace              | -4.6           | 60.5 $\pm$ 9.1      | 1119 $\pm$ 34       | 1687 $\pm$ 41        | 32.36          | 24.9           | 20.4            | 3.2   | 39.6              | 6.21  |
| NGC 5044 | Temi                | -4.7           | 23.0 $\pm$ 5.3      | 230 $\pm$ 14        | 242 $\pm$ 18         | 32.36          | 78.6           | 23.1            | 3.6   | 53.6              | 8.4   |
| NGC 5077 | Fazio               | -4.8           | 32.4 $\pm$ 5.7      | 127 $\pm$ 11        | 141 $\pm$ 13         | 32.36          | 25.0           | 20.2            | 3.2   | 49.5              | 7.8   |
| NGC 5322 | Fazio               | -4.8           | 41.4 $\pm$ 6.4      | 455 $\pm$ 23        | 625 $\pm$ 27         | 29.79          | 35.2           |                 |       |                   |       |
| NGC 5557 | Surace              | -4.8           | 13.2 $\pm$ 5.0      | 25.1 $\pm$ 10.5     | < 42                 | 49.02          | 28.6           |                 |       |                   |       |
| NGC 5813 | Fazio               | -4.8           | 14.9 $\pm$ 4.9      | 58.4 $\pm$ 7.6      | 34.8 $\pm$ 5.9       | 30.78          | 48.6           | 19.6            | 2.9   | 49.8              | 7.4   |
| NGC 5846 | Fazio               | -4.7           | 38.5 $\pm$ 6.2      | 102 $\pm$ 10        | 117 $\pm$ 12         | 24.55          | 82.6           | 20.4            | 2.4   | 43.1              | 5.1   |
| NGC 5982 | Surace              | -4.8           | 13.5 $\pm$ 5.1      | 37.2 $\pm$ 7.2      | 59.9 $\pm$ 11.7      | 40.18          | 29.4           |                 |       |                   |       |
| NGC 6703 | Fazio               | -2.8           | 19.9 $\pm$ 4.5      | 41.4 $\pm$ 6.4      | 17.9 $\pm$ 5.1       | 32.06          | 23.8           |                 |       |                   |       |
| NGC 7619 | Temi                | -4.7           | 9.9 $\pm$ 4.7       | < 3.8               | < 14.5               | 42.85          | 32.1           |                 |       |                   |       |
| IC 3370  | Kaneda              | -4.7           | 43.8 $\pm$ 6.7      | 649 $\pm$ 25        | 873 $\pm$ 30         | 45.90          | 18.5           | 20.5            | 4.5   | 39.7              | 8.8   |

<sup>a</sup> Galaxies are selected from the following Spitzer observing programs: SINGS Legacy Program, R. Kennicutt (PI); GTO program number 69, G. Fazio (PI); GO program number 3403, J. Surace (PI); GO program number 3506, Sparks (PI); GO program number 3619, H. Kaneda (PI); GO program number 3649, P. Cote' (PI); GO program number 20171, P. Temi (PI).

<sup>b</sup> The morphological type T is taken from the HyperLeda database.

<sup>c</sup> Distances are calculated with  $H_0 = 70 \text{ km s}^{-1} \text{ Mpc}^{-1}$ .

TABLE 2

| Name     | Log $L_{24}^a$<br>(erg/sec) | Log $L_{70}^a$<br>(erg/sec) | Log $L_{160}^a$<br>(erg/sec) | Log $L_B^a$<br>( $L_{B,\odot}$ ) | Log $L_X^a$<br>(erg/sec) | age <sup>b</sup><br>(Gyr) | Z <sup>b</sup><br>(dex)  |
|----------|-----------------------------|-----------------------------|------------------------------|----------------------------------|--------------------------|---------------------------|--------------------------|
| NGC 507  | ...                         | < 40.30                     | ...                          | 11.02                            | 42.76                    | 8.1±1.9                   | 0.261±0.071              |
| NGC 533  | 41.04                       | 41.19                       | 40.76                        | 10.96                            | 42.29                    | ...                       | ...                      |
| NGC 584  | 40.95                       | 40.59                       | < 39.66                      | 10.42                            | < 40.15                  | 2.8±0.3                   | 0.478±0.046              |
| NGC 596  | 40.48                       | 40.23                       | 39.65                        | 10.27                            | < 39.66                  | 2.8±0.4                   | 0.360±0.035              |
| NGC 636  | 40.29                       | < 40.11                     | < 39.82                      | 10.06                            | < 40.17                  | 4.4±0.6                   | 0.376±0.028              |
| NGC 720  | 40.62                       | 40.10                       | < 39.70                      | 10.44                            | 40.67                    | 5.4±2.4                   | 0.485±0.083              |
| NGC 855  | 40.38                       | 41.27                       | 41.00                        | 8.95                             | < 39.83                  | ...                       | ...                      |
| NGC 1377 | 42.48                       | 42.59                       | 41.81                        | 9.60                             | ...                      | ...                       | ...                      |
| NGC 1395 | 40.86                       | 40.94                       | 40.65                        | 10.50                            | 40.95                    | 7.6±1.4                   | 0.439±0.033              |
| NGC 1399 | 40.87                       | 39.92                       | 39.64                        | 10.58                            | 41.69                    | ...                       | ...                      |
| NGC 1404 | 40.85                       | 40.56                       | < 39.76                      | 10.41                            | 41.25                    | ...                       | ...                      |
| NGC 1407 | 40.83                       | < 28.83                     | < 39.91                      | 10.64                            | 41.06                    | 7.4±1.8                   | 0.379±0.044              |
| NGC 1700 | 40.95                       | 40.77                       | 40.44                        | 10.55                            | 40.66                    | 2.6±0.3                   | 0.500±0.049              |
| NGC 2325 | 40.96                       | 40.71                       | 40.01                        | 10.66                            | 40.76                    | ...                       | ...                      |
| NGC 2768 | 40.88                       | 41.68                       | 40.95                        | 10.63                            | 40.44                    | 10.0±7.0 <sup>c</sup>     | 0.14±0.25 <sup>c</sup>   |
| NGC 2974 | 41.27                       | 41.94                       | 41.94                        | 10.56                            | 40.64                    | ...                       | ...                      |
| NGC 2986 | 40.68                       | < 39.61                     | < 39.86                      | 10.57                            | 41.02                    | 11.2±1.9                  | 0.347±0.045              |
| NGC 3265 | 41.69                       | 42.15                       | 41.76                        | 9.46                             | ...                      | ...                       | ...                      |
| NGC 3379 | 40.39                       | 39.98                       | 39.51                        | 10.12                            | < 39.60                  | 10.0±1.1                  | 0.299±0.036              |
| NGC 3557 | 41.08                       | 41.64                       | 41.15                        | 10.82                            | 40.64                    | ...                       | ...                      |
| NGC 3610 | 40.71                       | 40.36                       | 40.13                        | 10.46                            | 39.89                    | 1.7±0.1 <sup>c</sup>      | 0.76±0.16 <sup>c</sup>   |
| NGC 3923 | 40.71                       | 40.06                       | 39.88                        | 10.58                            | 40.72                    | 3.3±0.8                   | 0.623±0.070              |
| NGC 3962 | 40.58                       | 41.45                       | 41.10                        | 10.34                            | < 40.28                  | ...                       | ...                      |
| NGC 4125 | 41.14                       | 41.92                       | 41.71                        | 10.86                            | 41.0                     | ...                       | ...                      |
| NGC 4365 | 40.32                       | 40.41                       | 39.86                        | 10.40                            | 40.31                    | 7.9±1.2 <sup>d</sup>      | 0.344±0.065 <sup>d</sup> |
| NGC 4472 | 40.85                       | 40.37                       | 39.92                        | 10.96                            | 41.49                    | 9.6±1.4                   | 0.342±0.046              |
| NGC 4552 | 40.74                       | 40.57                       | 40.37                        | 10.35                            | 40.77                    | 12.4±1.5                  | 0.356±0.034              |
| NGC 4589 | 40.53                       | 41.40                       | 41.07                        | 10.39                            | 40.42                    | ...                       | ...                      |
| NGC 4621 | 40.52                       | 40.11                       | 39.78                        | 10.38                            | 40.08                    | 8.8±1.1 <sup>d</sup>      | 0.299±0.050 <sup>d</sup> |
| NGC 4636 | 40.48                       | 40.88                       | 40.37                        | 10.57                            | 41.65                    | 10.3±1.3 <sup>d</sup>     | 0.181±0.104 <sup>d</sup> |
| NGC 4649 | 41.01                       | 40.27                       | < 39.57                      | 10.79                            | 41.34                    | 14.1±1.5                  | 0.362±0.029              |
| NGC 4660 | 40.16                       | 40.17                       | 39.87                        | 9.80                             | < 39.45                  | ...                       | ...                      |
| NGC 4696 | 41.07                       | 41.44                       | 41.30                        | 10.99                            | 43.23                    | ...                       | ...                      |
| NGC 4697 | 40.58                       | 41.33                       | 40.98                        | 10.61                            | 40.18                    | 8.3±1.4                   | 0.148±0.043              |
| NGC 4915 | 40.92                       | 40.95                       | 40.76                        | 10.34                            | < 40.93                  | ...                       | ...                      |
| NGC 5018 | 41.32                       | 42.21                       | 41.92                        | 10.63                            | < 40.59                  | ...                       | ...                      |
| NGC 5044 | 40.90                       | 41.52                       | 41.08                        | 10.76                            | 42.80                    | ...                       | ...                      |
| NGC 5077 | 41.05                       | 41.27                       | 40.85                        | 10.32                            | 40.54                    | ...                       | ...                      |
| NGC 5322 | 41.08                       | 41.75                       | 41.42                        | 10.73                            | 40.27                    | ...                       | ...                      |
| NGC 5557 | 41.02                       | 40.92                       | < 40.68                      | 10.90                            | ...                      | ...                       | ...                      |
| NGC 5813 | 40.67                       | 40.89                       | 40.20                        | 10.70                            | ...                      | 16.6±2.2                  | 0.059±0.042              |
| NGC 5846 | 40.88                       | 40.93                       | 40.53                        | 10.72                            | 41.71                    | 14.2±2.2                  | 0.226±0.051              |
| NGC 5982 | 40.86                       | 40.92                       | 40.66                        | 10.59                            | 41.22                    | ...                       | ...                      |
| NGC 6703 | 40.83                       | 40.77                       | 39.93                        | 10.43                            | < 40.09                  | 4.8±0.8                   | 0.354±0.034              |
| NGC 7619 | 40.78                       | < 39.99                     | < 39.96                      | 10.64                            | 41.69                    | 15.4±1.4                  | 0.291±0.031              |
| IC 3370  | 41.48                       | 42.28                       | 41.94                        | 10.82                            | ...                      | ...                       | ...                      |

<sup>a</sup> Luminosities are calculated with  $H_0 = 70 \text{ km s}^{-1} \text{ Mpc}^{-1}$ .<sup>b</sup> Ages and metallicities are taken from Thomas et al. 2005, unless otherwise stated.<sup>c</sup> Age and metallicity for this galaxy are taken from Howell 2005.<sup>d</sup> Age and metallicity for this galaxy are taken from Sanchez-Blazquez et al. 2006.

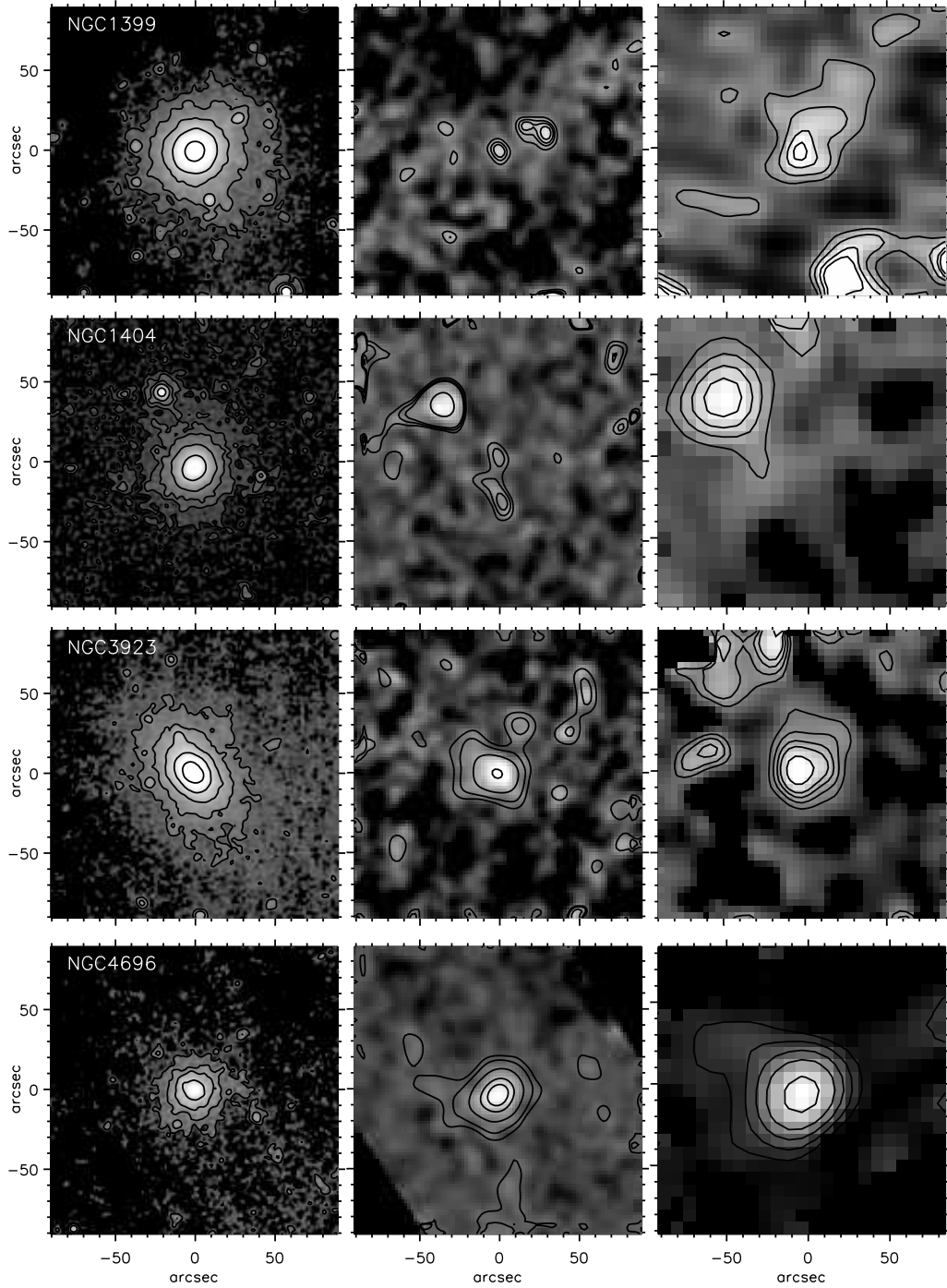
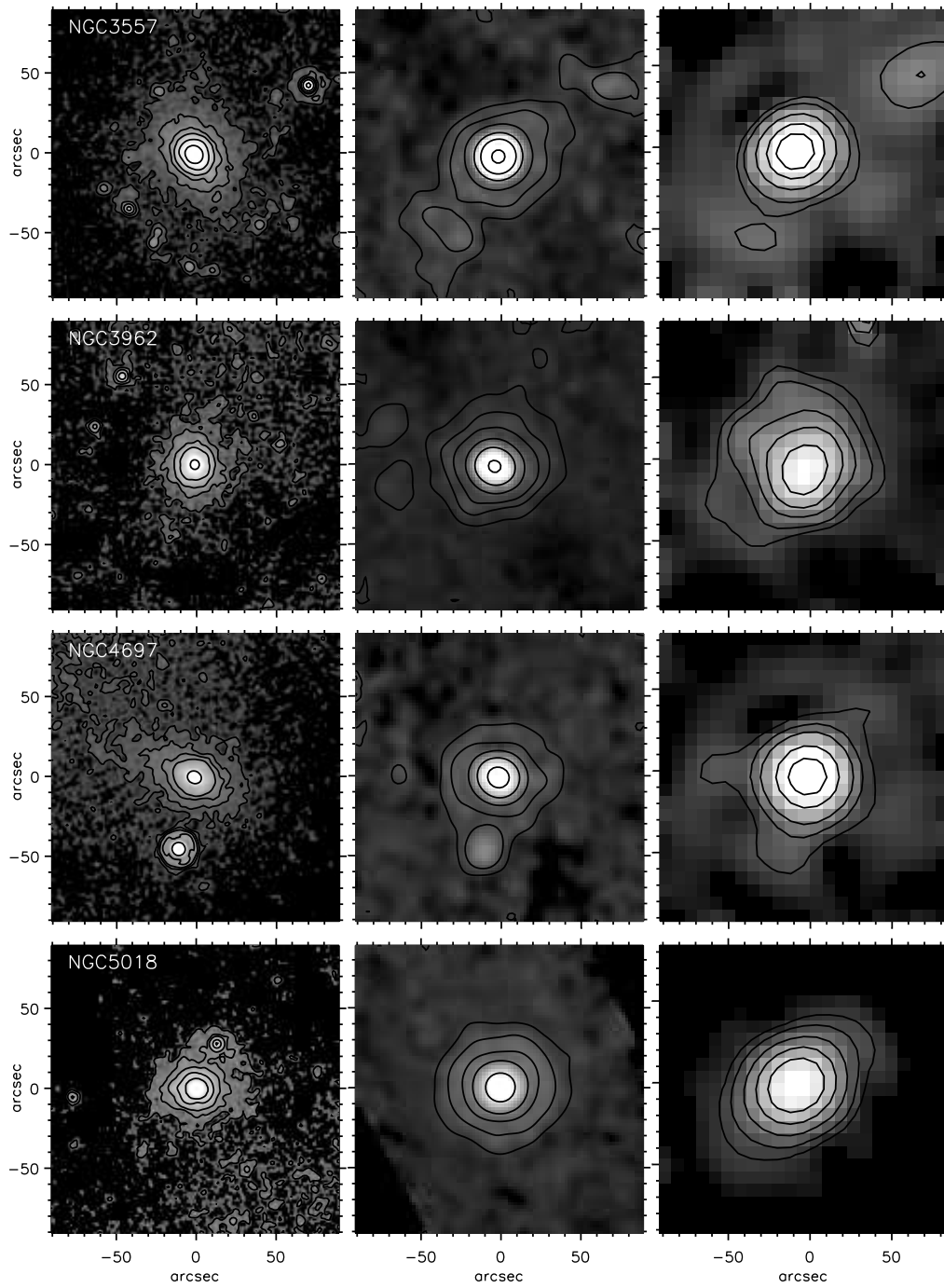


FIG. 1.— Grey scale images and contour plots of a representative sub-sample of Ellipticals. Each galaxy is shown in the three MIPS passbands centered at 24  $\mu\text{m}$  (left column), 70  $\mu\text{m}$  (center column), and 160  $\mu\text{m}$  (right column). Galaxies are shown in ascending order from lowest flux density to highest flux density, including a non detection and sources with extended far-infrared emission. The contour levels decrease by factors of 2 from the central peak value.

FIG. 1.— - *Continued*

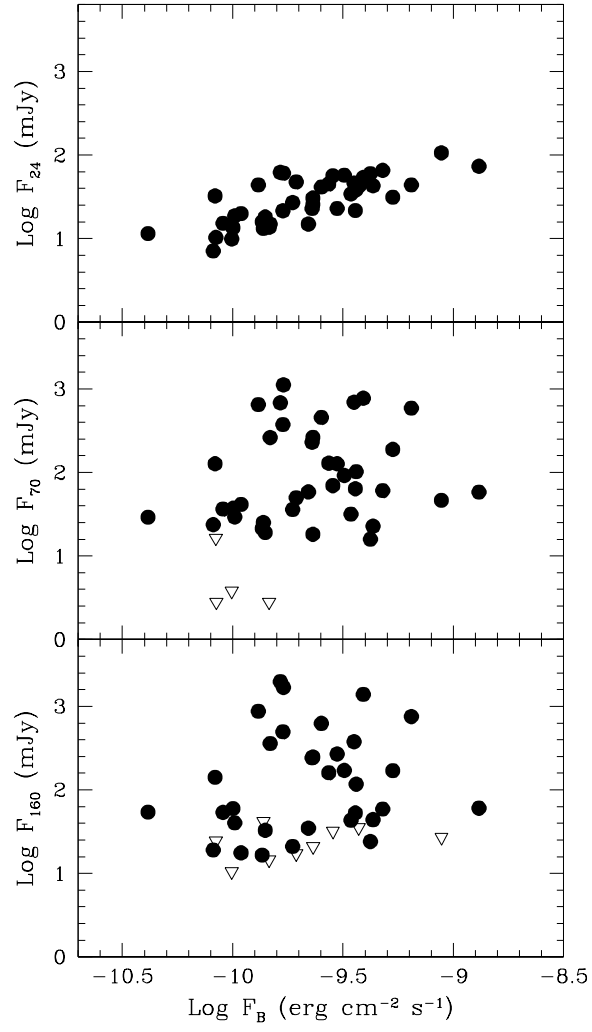


FIG. 2.— Comparison of fluxes at 24, 70 and 160 $\mu\text{m}$  with optical B-band fluxes. Downward pointing open arrows indicate upper limits.

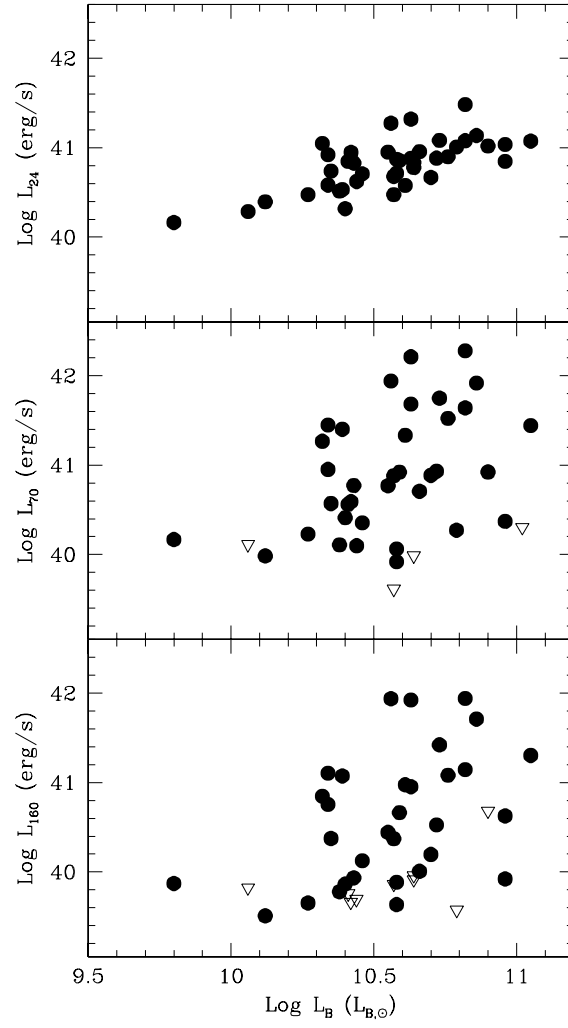


FIG. 3.— Comparison of luminosities at 24, 70 and 160  $\mu\text{m}$  with optical B-band luminosities. Downward pointing open arrows indicate upper limits.

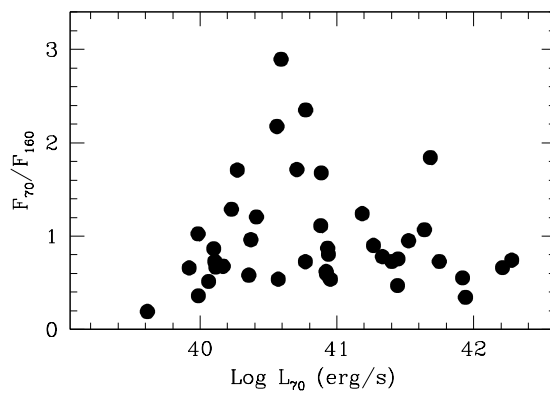


FIG. 4.— Comparison of  $F_{70}/F_{160}$ , a measure of dust temperature, with  $L_{70}$ .



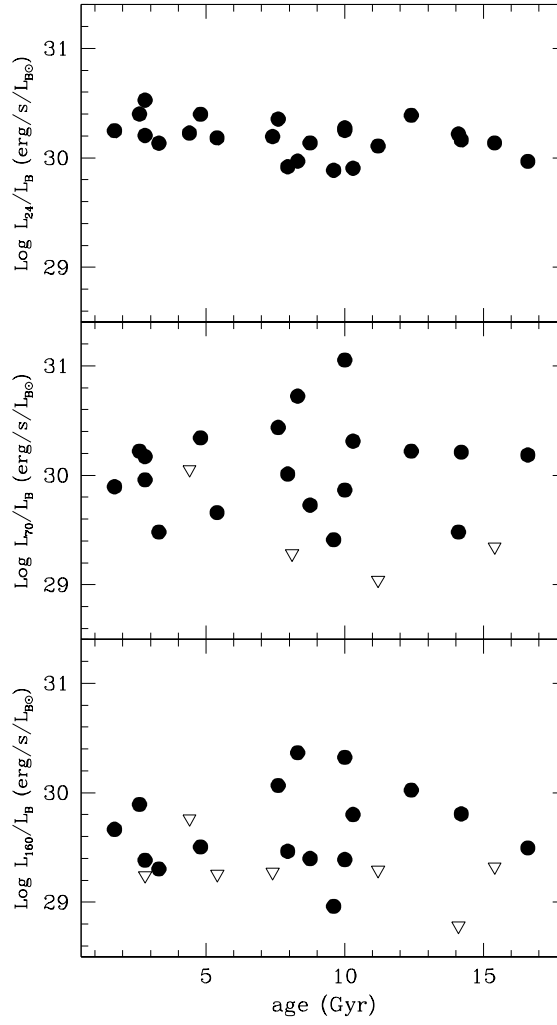


FIG. 5.— FIR to optical luminosity (or flux) ratios plotted against apparent stellar age from optical line indices.

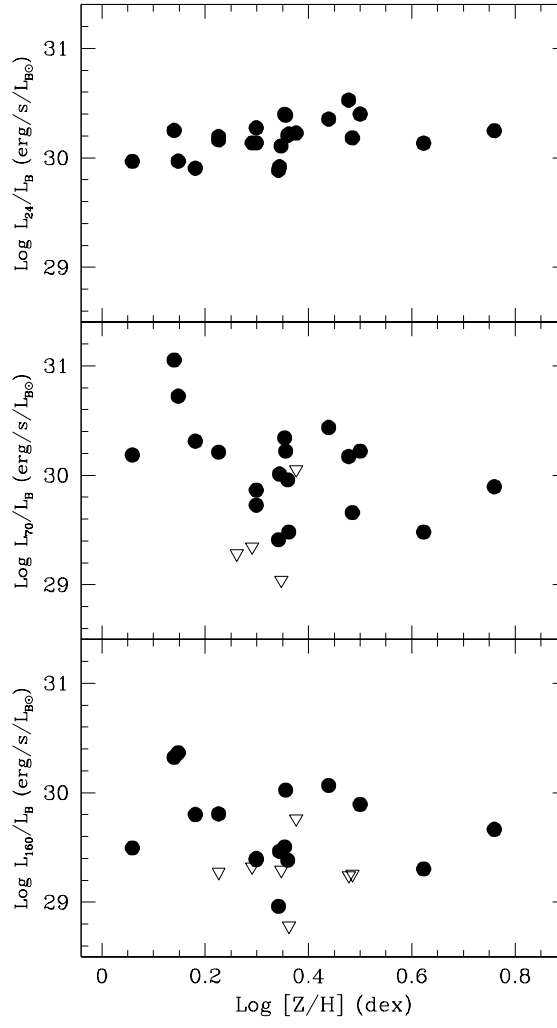


FIG. 6.— FIR to optical luminosity (or flux) ratios plotted against apparent stellar metallicity from optical line indices.

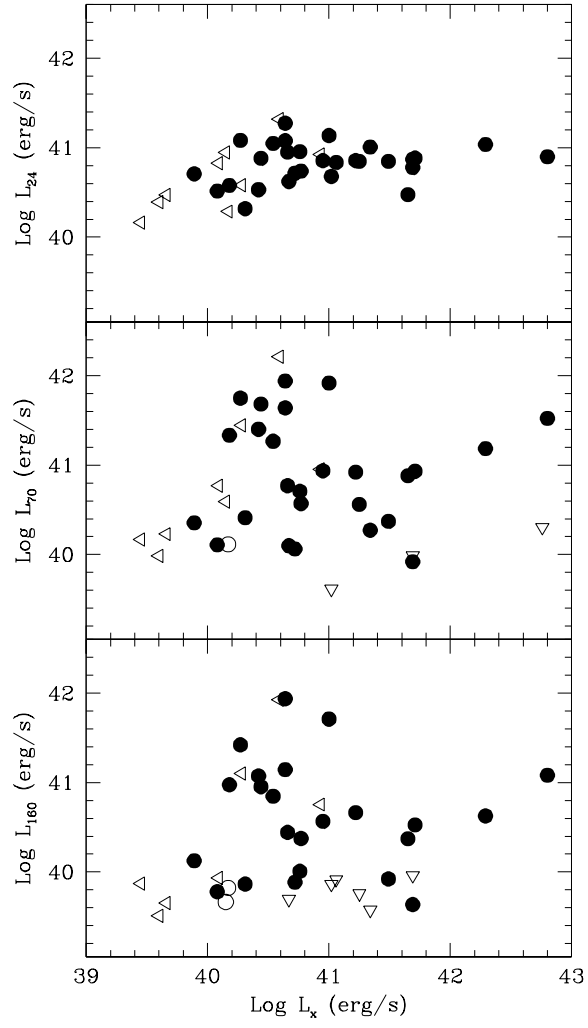


FIG. 7.— Comparison of FIR and X-ray bolometric luminosities.

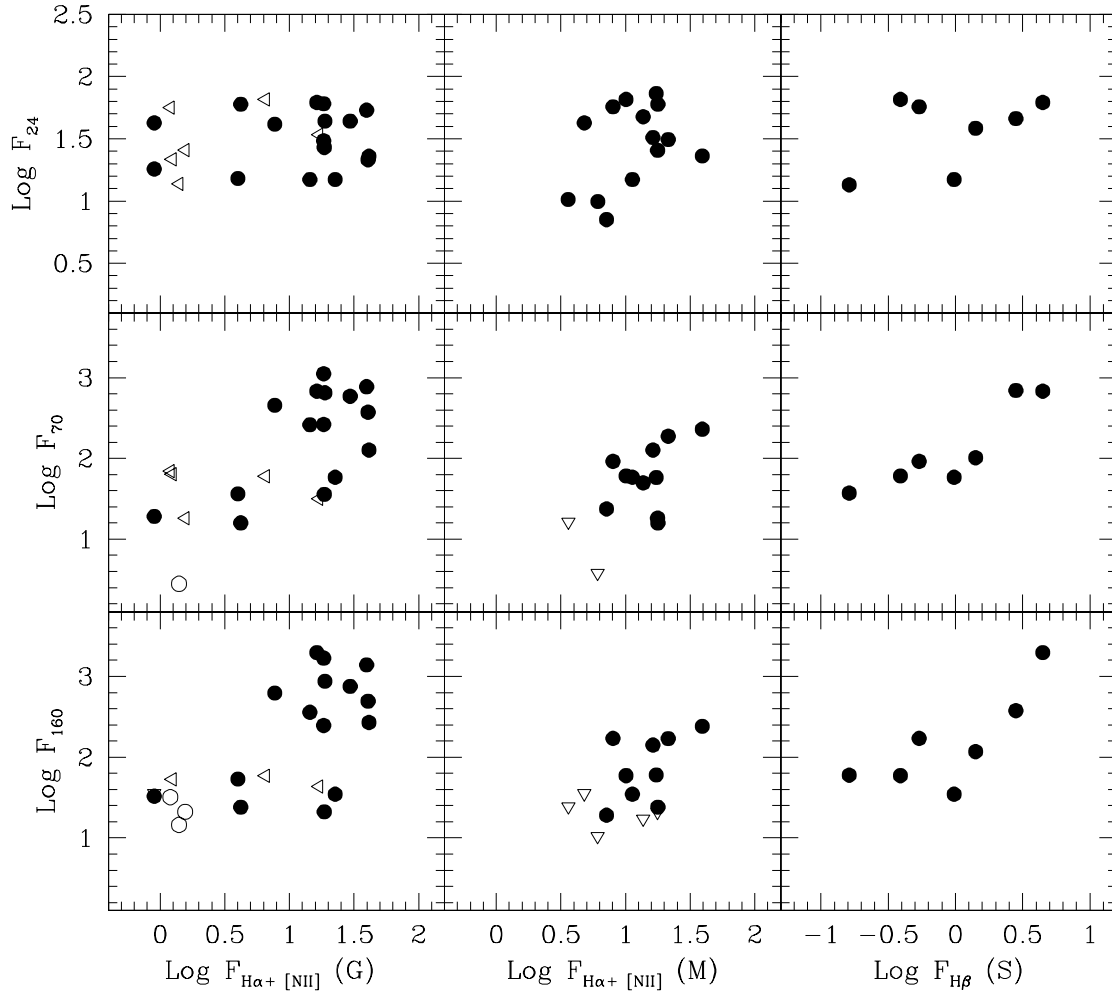


FIG. 8.— FIR fluxes plotted against fluxes in optical line emission. From left to right the three-panel columns refer respectively to data from Goudfrooij (1994a,b), Macchetto et al. (1996), and Sarzi et al. (2006). Open triangles indicate upper limits in the direction they are oriented and open circles are upper limits in both coordinates.

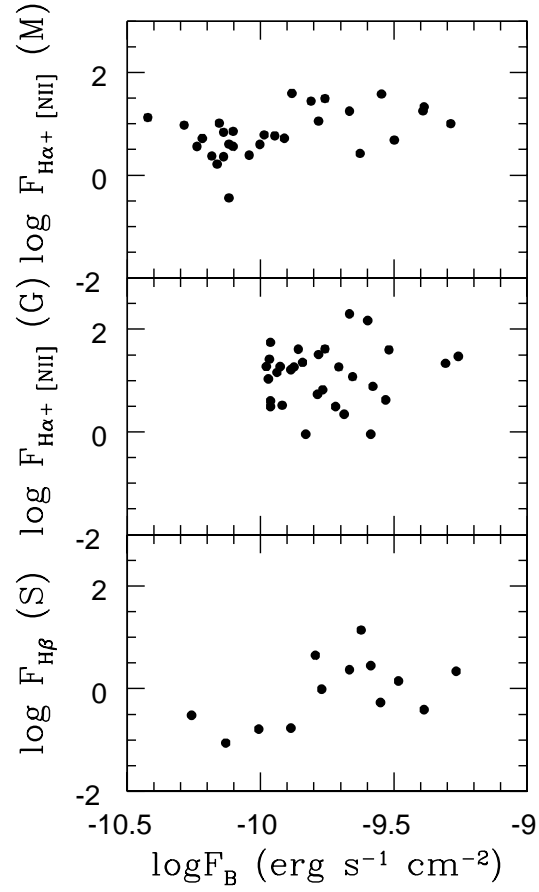


FIG. 9.— Comparison of B-band fluxes with optical emission line fluxes in units of  $10^{-14}$   $\text{erg s}^{-1} \text{cm}^{-2}$ . The optical fluxes are taken from (G) Goudfrooij (1994a,b), (M) Macchetto et al. (1996), and (S) Sarzi et al. (2006) Only non-peculiar E and E/S0 galaxies are plotted.

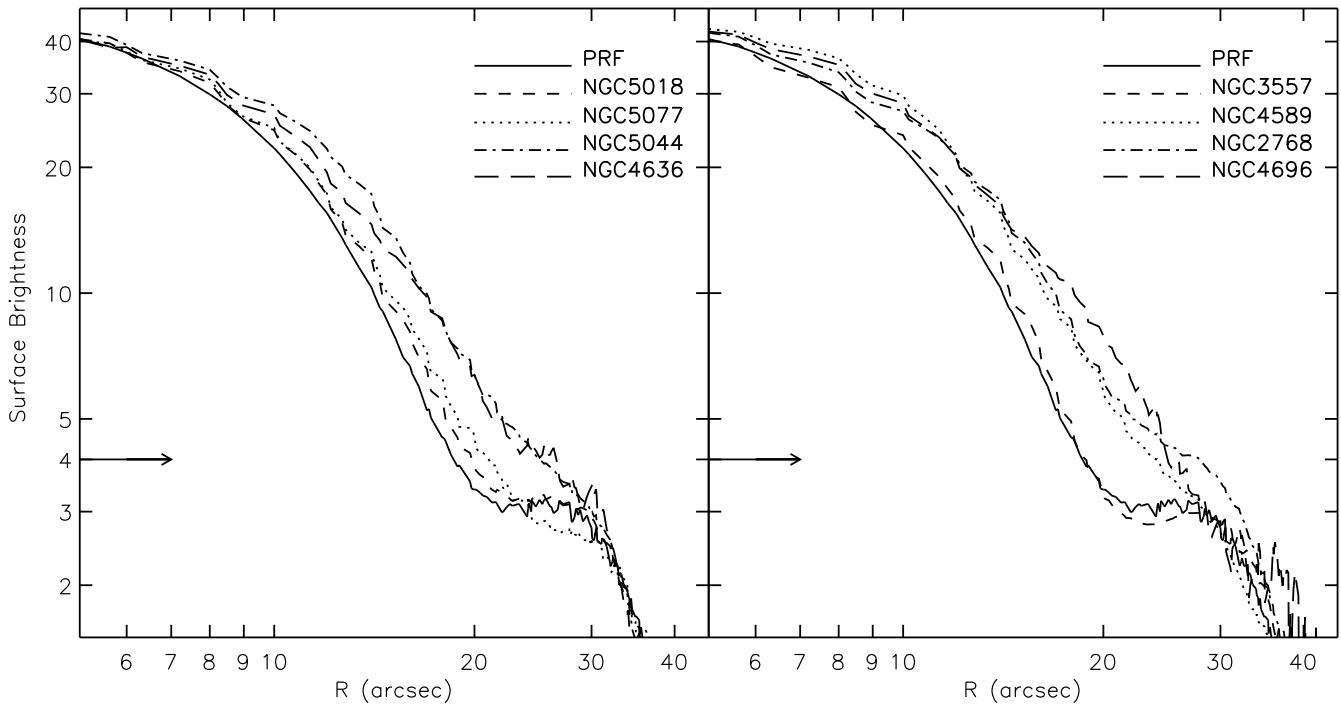


FIG. 10.— Surface brightness distributions at  $70\mu\text{m}$  (in arbitrary units) for eight galaxies compared to the point response function (PRF) of the MIPS detector. All curves are normalized to 50. at the center and the arrows show the level at 0.1 of the maximum.

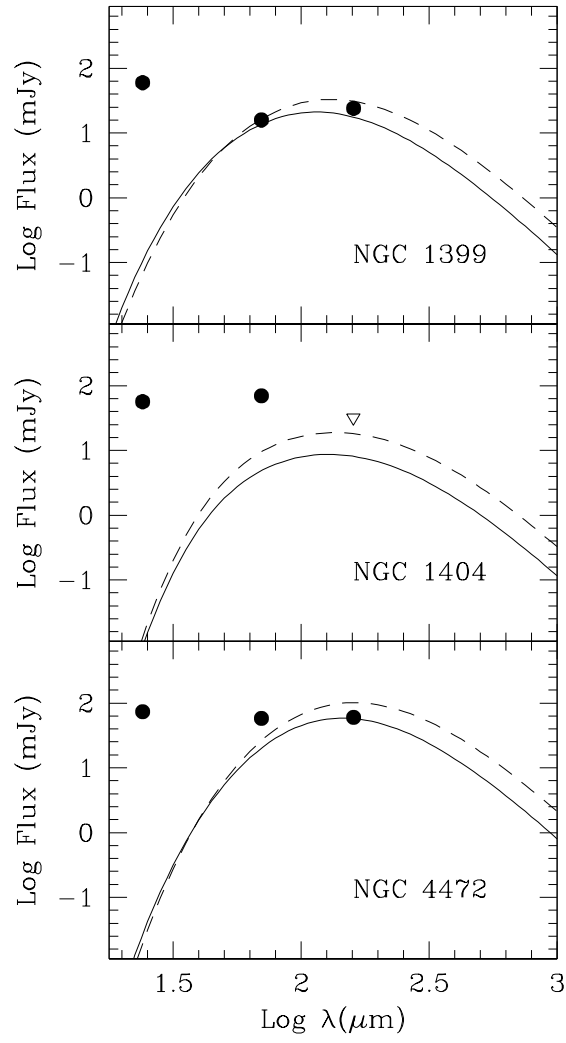


FIG. 11.— Comparison of 24, 70 and  $160 \mu\text{m}$  fluxes with the our model spectral energy distributions. The open triangle is an upper limit of  $F_{160}$  for NGC 1404. The solid and dashed lines correspond respectively to emission from grains with original maximum sizes  $a_{max} = 0.3 \mu\text{m}$  and  $1.0 \mu\text{m}$ .

## APPENDIX

## NATURE OF FIR-LUMINOUS GALAXIES

In this appendix we briefly review other observations of galaxies in Figure 3 and Table 2 having the most luminous FIR emission. Our objective is to determine if elliptical galaxies with the most luminous FIR emission can be regarded as unusual or abnormal and, if so, what is the maximum FIR luminosity of sample galaxies that can be regarded as normal. In the following we emphasize observations that are consistent with large FIR emission – evidence of large ( $\sim 10$  kpc) extended dusty disks, detections of large masses of cold gas or recent star formation, designations as an S0 galaxy which often contain cold, rotationally supported gaseous disks, strong radio emission, galaxies with nearby dusty galaxies or stars that may have contaminated some observations, evidence of a recent merger, etc. – but we do not mention attributes that are found in many typical ellipticals: extended optical emission lines perhaps with a LINER spectrum, small central ( $\lesssim 1$  kpc) dust clouds that obscure starlight, weak central radio sources, X-ray emission  $L_x$  which is highly variable among ellipticals, evidence of old mergers, etc. Galaxies are listed in descending order of  $L_{70}$ .

**IC 3370:** Classified as an elliptical in RC2 an RSA, but regarded by Jarvis (1987) and Samurovic & Danziger (2005) as an S0 or S0pec with an extremely boxy profile. A bright IRAS source in FIR. Richter et al. (1994) detect an HI mass of  $5 \times 10^8 M_\odot$ . Contains a prominent dust lane in the inner regions with associated H $\alpha$  + [NII] emission and possible evidence of ongoing star formation (Michard 2006). Leonardi & Worthey (2000) and Tantaló & Chiosi (2004) suggest an intermediate age population for the central regions.

**NGC 5018:** Forms a pair with NGC 5022 7.2' away. Carollo & Danziger (1994) describe a very strong dust lane that obscures the innermost regions that may contain recent star formation. They also suggest that the galaxy is very flat (about E6). Detected by IRAS at 60 and 100 $\mu$ m. Xilouris et al. (2004) find excess MIR emission at 6.7 and 15 $\mu$ m, perhaps suggesting heating by recent star formation.

**NGC 2974:** A rapidly rotating E4 galaxy (Emsellem et al. 2004). Strong IRAS emission. Kim et al. (1988) observes a massive HI disk,  $M_{HI} = 2 \times 10^9 M_\odot$  (with  $D = 38$  Mpc). Sarzi et al. (2006) observe a nuclear bar with two spiral arms emerging. A bright star is seen in NED images 0.7' to SW.

**NGC 4125:** Filho et al. (2002) regard this as an E6pec galaxy. Wickland et al. (1995) detect tentative molecular hydrogen emission with mass  $M_{H_2} = 7 \times 10^7 M_\odot$ . Verdoes Kleijn & de Zeeuw (2005) observe a central dust lane of size 160 pc ( $D = 26$  Mpc).

**NGC 5322:** Carollo et al. (1997) describe a completely obscuring dust lane (perpendicular to the radio jet) that hides the center of the galaxy. IRAS detection at 60 and 100 $\mu$ m. Proctor & Sansom (2002) and Denicolo et al. (2005) find evidence of a  $\sim 2 - 4$  Gyr old young stellar population.

**NGC 2768:** Referred to as an E6\* in RC3, this is almost certainly an S0 galaxy (Funes et al. 2002) with faint dust patches surrounding the galactic bulge. Significant dust extinction is visible along the minor axis (Michard 1999). Bertola et al. (1992) notes that the ionized gas is dynamically decoupled from the stars, which may be related to gas orbiting in a polar ring (Mollenhoff et al. 1992; Fried & Illingworth 1994). Wiklind et al. (1995) observed CO emission with an estimated molecular mass of  $\sim 2 \times 10^7 M_\odot$ .

**NGC 3557:** An E3 galaxy containing an FRI radio source having a double-tailed radio source with a jet and central knot (Birkinshae & Davies 1985). Detected by IRAS at 60 and 100 $\mu$ m. Rampazzo et al. (2005) report a possible dust ring near the center and Goudfrooij (1994b) finds an unusual optical emission line image associated with the minor axis.

**NGC 5044:** Detected by IRAS at 60 and 100 $\mu$ m. Very bright and asymmetrically extended optical emission (Ferrari, et al. 1999; Goudfrooij et al. 1994a).

**NGC 3962:** The H $\alpha$ + [NII] image shows two sub-systems: an elongated (dusty) central component strongly misaligned with the stellar isophotes extending to  $\sim 7$  kpc with regular kinematics and a more extended arm-like structure associated with bluer stars (Buson et al. 1993; Goudfrooij, et al. 1994b; Zeilinger et al. 1996). Detected by IRAS at 60 and 100 $\mu$ m.

**NGC 4589:** Prominent dust lane near minor axis extending to 20'' (Goudfrooij, et al. 1994a,b) Complex gas and stellar kinematics suggest a merger remnant (Mollenhoff & Bender 1989). Detected by IRAS at 60 and 100 $\mu$ m.

**NGC 4697:** An E6 galaxy, but may be an S0 (Koprolin & Zeilinger 2000). Sofue and Wakamatsu (2003) detect a molecular mass of  $3 \times 10^7 M_\odot$ .



**NGC 5077:** The E3 designation in RC2 is wrong, this is an S0 galaxy (Sandage & Bedke 1994).

## ESTIMATED FIR EMISSION FROM CENTRAL OPTICALLY THICK CLOUD

In this Appendix we determine if a large fraction of the FIR emission from elliptical galaxies can come from small, dense, dusty clouds near the centers of the galaxy, or, as we have generally assumed, comes from FIR-emitting dust diffusely distributed throughout the inner galaxy. Specifically, can reprocessed starlight from internal and external stars heat small dusty regions sufficiently to account for the large FIR luminosities shown in Figure 3? We describe a simple calculation to estimate the maximum luminosity at  $70\mu\text{m}$   $L_{70}$  expected from a small optically thick dust cloud, including dust heating by both internal and external starlight.

Consider a spherical cloud of dusty cold gas with radius  $r_c$  placed at the center of an elliptical galaxy having a de Vaucouleurs luminosity profile. Since the stellar density is greatest at the center, placing the cloud there maximizes the energy from internal starlight that can be absorbed and reemitted at infrared wavelengths. The mean intensity of starlight in an (optically thin) elliptical galaxy also is greatest at the galactic center, where the stellar flux incident on the dusty cloud from the outside is also maximal.

Without investigating in detail how the dust is heated and reemitted in the infrared from small, dense clouds, we assume that this type of reprocessing can occur. To estimate the fraction of the the FIR that appears in the *Spitzer*  $70\mu\text{m}$  pass band, we assume that the overall infrared SED can be approximated with a modified blackbody, with emissivity  $j_{nu} \propto \nu^\beta B_{nu}(T_d)$  where  $\beta$  depends on the properties of the dust and  $T_d$  is the dust temperature. We assume  $\beta = 1$  and  $T_d = \langle T_d \rangle = 27.9\text{K}$ , the mean values in our SED fits to ISO (*Infrared Space Observatory*) FIR data for elliptical galaxies (Temi et al. 2004). The fraction of FIR emission that emerges in the *Spitzer*  $70\mu\text{m}$  passband (width  $\Delta\lambda_{70} = 19\mu\text{m}$ ) is

$$\frac{L_{70}}{L_{FIR}} = \frac{\int_{\Delta\nu_{70}} \nu^\beta B_\nu(\langle T_d \rangle) d\nu}{\int_0^\infty \nu^\beta B_\nu(\langle T_d \rangle) d\nu} = 0.147 \quad (\text{B1})$$

where  $\Delta\nu_{70} = c\Delta\lambda_{70}/\lambda_{70}^2$ .

To be specific we consider a typical elliptical in Figure 3 with  $\log L_B = 10.6$ . Based on the galaxy-size observations of Shen et al. (2003), we assume a typical effective radius for this galaxy,  $r_e = 7.67$  kpc. To determine the total B-band luminosity of stars inside the dusty cloud, we integrate the de Vaucouleurs profile from the center to radius  $r_c$ . To convert the B-band luminosity to bolometric luminosity of an old single stellar population (SSP), we assume solar abundance for the stars, a Kroupa IMF and an age of  $10^{10}$  yrs, resulting in  $(L_B/L_{B\odot})/(L_{bol}/L_{bol,\odot}) = 0.396$  (private communication from Justin Harker). With this information we can estimate the total stellar luminosity produced within a dusty cloud of any chosen radius  $r_c$  and the fraction of this energy that is observed in the *Spitzer*  $70\mu\text{m}$  passband,  $L_{70}(int)$ .

The dusty cloud can also be heated externally by stellar radiation incident on its outer surface. To estimate the flux of stellar radiation incident on the dusty cloud we first determine the mean B-band mean intensity within 10-100 parsecs of the galactic center,  $J_B \approx 0.03 \text{ erg cm}^{-2} \text{ s}^{-1} \text{ ster}^{-1}$ , found by integrating over the de Vaucouleurs emissivity profile corresponding to  $L_B = 10^{10.6} L_{B\odot}$  and  $r_e = 7.67$  kpc. The B-band flux on the surface of the cloud is then  $F_B = \pi J_B$ . The bolometric flux is larger by a factor  $F_{bol,\odot}/F_{B,\odot} = 1/0.396$  so the rate that radiative energy from external galactic stars is absorbed by the dusty cloud is  $L_{70}(ext) = a4\pi r_c^2 (F_B/0.396)$  where  $a = 0.5$  is the assumed albedo.

Figure B1 shows how the  $70\mu\text{m}$  luminosities  $L_{70}(int)$  and  $L_{70}(ext)$  vary with the radius  $r_c$  of the dusty cloud where we see that  $L_{70}(ext) < L_{70}(int)$ . But the important result is that clouds of size  $r_c \sim 100$  pc are required to produce luminosities  $L_{70} \sim 10^{41} \text{ erg s}^{-1}$  typical of those plotted in the central panel of Figure 3. In many of the elliptical galaxies in Figure 3, a  $\sim 100$  parsec dark cloud would be easily visible even without HST resolution. We conclude that it is very unlikely that the large excess FIR emission in Figure 3 above that predicted by our simple model for recently produced diffuse dust, can be explained by emission from small dense clouds even under the most favorable circumstances.

More importantly, the approximation of spherical clouds is seriously in error. The gas temperatures associated with these dusty clouds ( $\sim 100\text{K}$ ?) are much less than the virial temperature of the stars,  $T_* \sim 10^6$  K required to support a spherical cloud as we hypothesized here. The gas temperature within the dusty cloud is insufficient to provide pressure support against the stellar potential due to embedded stars or the external hot gas pressure. Consequently, we expect that most of the nuclear dust clouds observed in ellipticals are highly flattened, nearly two-dimensional pancakes or disks. In this case we imagine that the  $L_{70}(ext)$  luminosities in Figure B1 are more relevant, further reducing the predicted  $70\mu\text{m}$  emission. We conclude that most of the FIR emission observed at  $70\mu\text{m}$  and  $160\mu\text{m}$  is diffusely distributed, not concentrated in dense clouds similar to those seen in absorption by many optical observers.

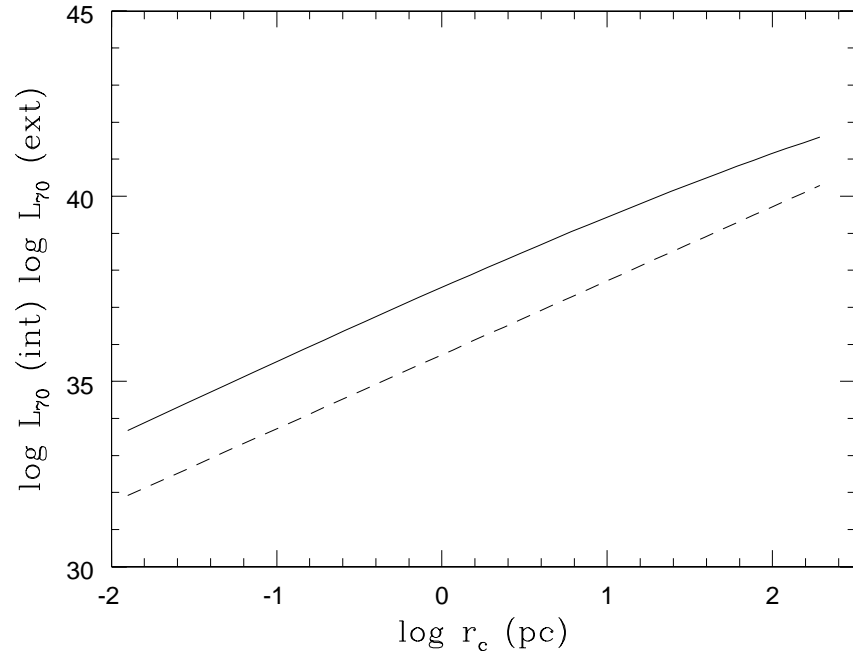


FIG. 12.— Estimated  $70\mu\text{m}$  luminosity emitted from an optically thick dust sphere located at the center of an elliptical galaxy having a de Vaucouleurs stellar luminosity with  $L_B = 10^{10.6} L_{B\odot}$  and  $r_e = 7.67$  kpc. As the cloud radius  $r_c$  is varied, the two curves show the  $70\mu\text{m}$  luminosity from reprocessed starlight emitted (and absorbed) within the dust cloud  $L_{70}(\text{int})$  (*solid line*) and the reprocessed luminosity absorbed by starlight incident on the sphere from galactic stars beyond  $r_c$ ,  $L_{70}(\text{ext})$  (*dashed line*).